

**Summer Project Report**

**Study of magnetization dynamics in  
Pt/CoFeB thinfilms**

Submitted by

**Gaurav Kanu  
1811067**

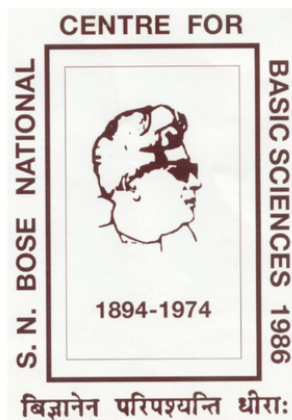
4th year Integrated MSc

National Institute of Science Education and Research

Under the guidance of

**Dr. Anjan Barman  
Professor**

Dept. of Condensed Matter Physics and Material Sciences  
S. N. Bose National Centre for Basic Sciences



SUMMER RESEARCH PROGRAMME - 2022

# Contents

<b>Acknowledgement</b>	<b>2</b>
<b>1 Introduction</b>	<b>3</b>
1.1 Micromagnetism . . . . .	4
1.1.1 Ferromagnetic domains . . . . .	4
1.1.2 Domain walls . . . . .	4
1.1.3 Magnetic anisotropy . . . . .	5
1.1.4 Effect of stress on magnetic anisotropy . . . . .	7
1.1.5 Hysteresis . . . . .	8
1.2 Exchange interactions . . . . .	9
1.2.1 Heisenberg exchange . . . . .	9
1.2.2 Dzyaloshinskii-Moriya Interaction (DMI): . . . . .	10
1.2.3 Anisotropy: . . . . .	10
1.2.4 Zeeman energy: . . . . .	10
1.2.5 Dipole-Dipole interaction . . . . .	11
1.2.6 Ruderman–Kittel–Kasuya–Yosida (RKKY) interaction	11
1.3 Magnetization dynamics . . . . .	11
1.3.1 Landau-Lifshitz-Gilbert equation . . . . .	12
<b>2 Laser induced magnetization dynamics</b>	<b>14</b>
2.1 Ultrafast demagnetization . . . . .	14
2.1.1 Elliot-Yafet (EY) scattering . . . . .	17
2.1.2 Coulomb scattering (EY-like mechanism without considering phonon bath) . . . . .	17
2.1.3 Magetization precession . . . . .	18
<b>3 Spin and Spin Current</b>	<b>21</b>
3.1 Spin Polarization . . . . .	21
3.2 Spin Current . . . . .	22
3.3 Hall effect . . . . .	23
3.3.1 Ordinary hall effect . . . . .	23

3.3.2	Anomalous Hall effect . . . . .	24
3.3.3	Spin Hall effect . . . . .	24
<b>4</b>	<b>Experimental technique</b>	<b>26</b>
4.1	Magneto-Optical Kerr Effect (MOKE) . . . . .	26
4.2	Theory of magneto-optical Kerr effect . . . . .	26
4.2.1	Physical Origin of Magneto-Optical Effects . . . . .	27
4.2.2	Phenomenological theory of MOKE . . . . .	28
4.3	MOKE Geometries . . . . .	30
4.4	Time resolved measurements . . . . .	31
4.4.1	Ultrafast pump-probe technique . . . . .	32
4.4.2	Precessional fitting: . . . . .	33
4.4.3	Effective magnetization: . . . . .	34
4.4.4	Effective damping: . . . . .	34
<b>5</b>	<b>Experimental setup</b>	<b>35</b>
5.1	Apparatus required . . . . .	35
5.1.1	Working mechanism . . . . .	36
5.2	Sample details and fabrication . . . . .	37
5.2.1	RF and DC Magnetron Sputtering System . . . . .	37
<b>6</b>	<b>Results and discussion</b>	<b>40</b>
6.1	Laser-induced ultrafast magnetization dynamics . . . . .	40
6.2	Fitting of experimental data and analysis of related parameters	40
6.2.1	Fitting and analysis of demagnetization data . . . . .	40
6.3	Fitting and analysis of precessional data . . . . .	45
6.3.1	Field dependent precessional data . . . . .	45
6.3.2	Fluence dependent precessional data . . . . .	51
<b>7</b>	<b>Conclusion</b>	<b>56</b>

# Certificate

This is certified that the project report "**Study of magnetization dynamics in Pt/CoFeB thinfilms**" being submitted by Gaurav Kanu (NISER, Bhubaneswar) under the supervision of Prof. Anjan Barman, to S. N. Bose National Centre for Basic Sciences , JD-Block, Sector III, Saltlake, Kolkata-700106, as a summer project under Summer Research Programme 2022. The results contained in this report have not been submitted elsewhere for any type of degree or any diploma course.

.....  
(Dr. Anjan Barman)

Date:

# Acknowledgment

I take this opportunity to express my sincere gratitude to Prof. Anjan Barman, (SNBNCBS, Salt lake, Kolkata) for giving me an opportunity to work under his guidance and supporting me during this entire period of the project, without which the completion of my project would not be possible.

I would also like to sincerely thank Mr. Surya Narayan Panda (SRF (Thesis submitted), SNBNCBS), Mrs. Suchetana Mukhopadhyay (JRF, SNBNCBS) for their valuable guidance on TR-MOKE and helping me throughout the whole project with all my doubts and ideas.

I would like to thank all the lab members (Sourav Kumar Sahoo(VRF (Thesis submitted)), Sudip Majumdar(SRF), Koustuv Dutta (SRF), Arundhati Adhikari (SRF), Amrit Kumar Mondal (SRF), Pratap Kumar Pal(SRF), Soma Dutta(SRF), Sreya Pal(SRF), Chandan Kumar (JRF), Rajdwip Bhar (IphD), Prapti Mukherjee (IphD), Dr. Arpan Bhattacharyya (Postdoc)) for always warmly welcoming all my doubts and helping me whenever I faced any problems.

# Chapter 1

## Introduction

In today's fast evolving technology world devices with fast operation time has become a basic requirement of people and each newly launched device influences market with its new features such as high read/write speed and higher memory. So keeping the requirements in mind researchers have keen interest to increase the density of storage, while maximizing the read and write speed of the device (i.e. the information transfer rate). Since the discovery of Giant Magneto Resistance (GMR) there has been significant improvement in data storage, but achieving high read and write speed within reasonable current supply is still one of the biggest challenge. The study magnetization dynamics is analysed at a very precise time scale of  $10^{-15} \text{ sec}$ , what one can best do is to formulate some theoretical model based on the understanding of what exactly can happen there and can predict the experimental findings. In this project we aim for studying a bilayer system of ferromagnet (FM) and non-magnet (NM) and measuring and analysing the underlying properties of the material such as damping, demagnetization time, remagnetization time with varying laser fluence and external field.

In this project we perform the measurements using Time Resolved Magneto Optical Kerr Effect (TR-MOKE). Magneto Optical effects in magnetic materials arise due to the optical anisotropy of the materials. The source of this optical anisotropy is the magnetisation ( $M$ ) within surface domains which can be influenced by external forces such as magnetic fields. The optical anisotropy alters the state of linearly polarised light which is reflected off magnetic materials. These effects are generally known as the Magneto-Optical Kerr Effect (MOKE) which were observed by John Kerr in 1887. Kerr effect being proportional to the magnetisation is particularly useful in the study of surface magnetism since it is highly sensitive to the magnetisation within the skin depth region, typically 10-20 nm in most metals.

## 1.1 Micromagnetism

### 1.1.1 Ferromagnetic domains

Ferromagnetic domains are small regions in ferromagnetic materials within which all the magnetic dipoles are aligned parallel to each other. When a ferromagnetic material is in its demagnetized state, the magnetization vectors in different domains have different orientations, and the total magnetization averages to zero.

#### Reason for many domains

In a ferromagnetic material the main reason for occurrence many domains is to reduce the magnetostatic energy, the below diagram depicts how division into smaller domains will help us to reduce the magenetostatic energy.

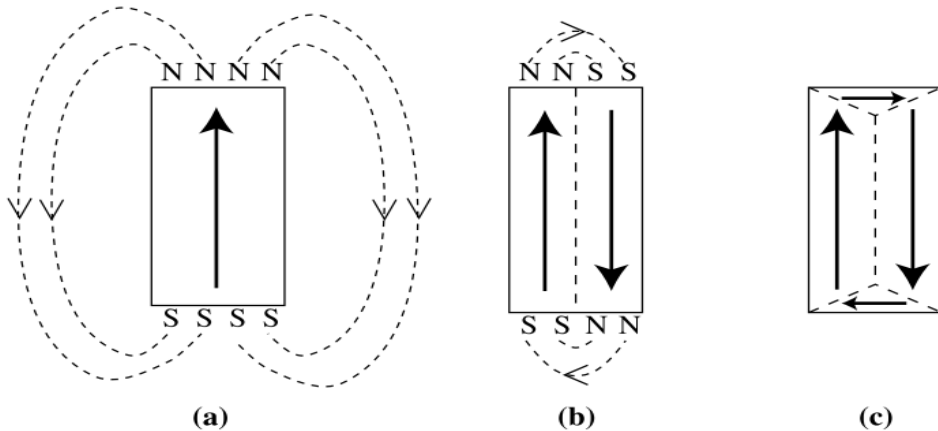


Figure 1.1: Reduction of the magnetostatic energy by domain formation in a ferromagnet.

[1]

### 1.1.2 Domain walls

Domain walls are the boundaries between the adjacent domains. The adjacent magnetization usually differ by  $90^\circ$  or  $180^\circ$ . There are two types of domain walls: (i) Bloch wall and (ii) Neel wall

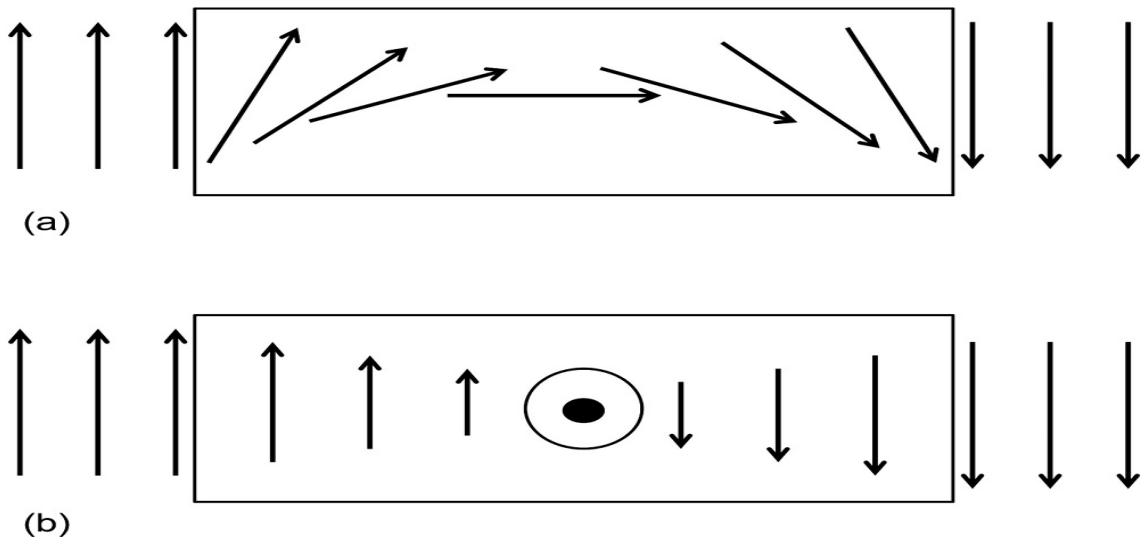


Figure 1.2: (a) Néel wall and (b) Bloch wall

### Néel and Bloch walls

In Néel wall the rotation of the magnetic moments takes place in plane whereas in Bloch wall rotation takes place is out of the plane. The Fig.2 shows the rotations in Néel wall and Bloch wall.

#### 1.1.3 Magnetic anisotropy

The dependence of the magnetic properties on the direction of the applied field with respect to the crystal lattice. Depending on the orientation of the field with respect to the crystal lattice one would need a lower or higher magnetic field to reach the saturation magnetization. There are several kinds of anisotropy:

- Magnetocrystalline anisotropy- It is intrinsic to the material. It is the energy required to deflect the magnetic moment in a crystal from the easy to the hard direction.
- Shape anisotropy- It is because of the dipolar interaction. This interaction is long range and so its contribution is dependent upon the shape of the sample.
- Stress anisotropy- Change in the anisotropy of the sample because of the strain on the material.

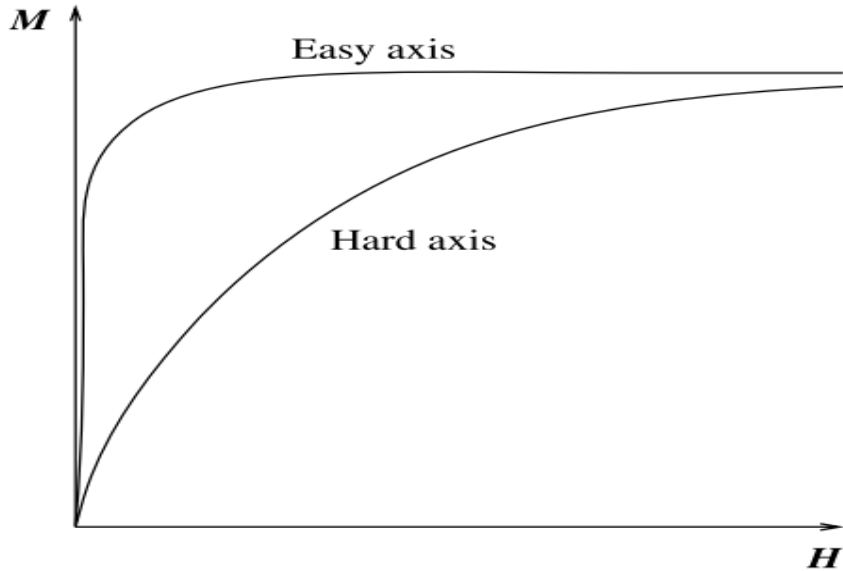


Figure 1.3: Fig.3: Schematic magnetization curves for a ferromagnet with the field oriented along the hard and easy directions[1].

- Exchange anisotropy - Exchange coupling at the interface between two different magnetically ordered systems.

### Magnetocrystalline energy

The magnetization in ferromagnetic crystals tends to align along certain preferred crystallographic directions. The preferred directions are called the “easy” axes, since it is easiest to magnetize a demagnetized sample to saturation if the external field is applied along a preferred direction.

Below plot shows the magnetization along easy axes and hard axes.

In both the case saturation magnetization is achieved but much larger applied field is required to reach saturation along the hard axis than along the easy axis.

#### Cubic crystal:

$$E_a = K_0 + K_1(\alpha_1^2\alpha_2^2 + \alpha_2^2\alpha_3^2 + \alpha_3^2\alpha_1^2) + K_2(\alpha_1^2\alpha_2^2\alpha_3^2) \quad (1.1)$$

$\alpha_1, \alpha_2, \alpha_3$  are the direction cosines,  $\alpha_i = \cos \theta_i$  and  $\theta_i$  are the angles between the magnetization and the easy axes.

$K_0, K_1, K_2$  are anisotropy constants. For a particular material at a particular temperature and are expressed in erg/cm<sup>3</sup> (cgs) or J/m<sup>3</sup> (SI).

#### Uniaxial crystal:

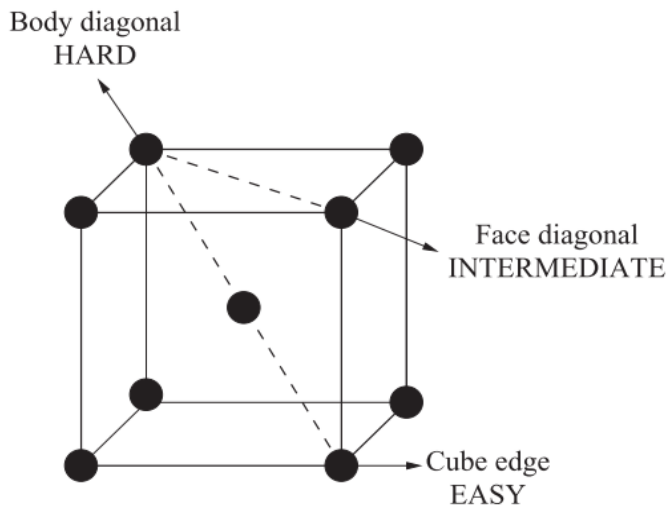


Figure 1.4: Easy, medium, and hard directions of magnetization in a unit cell of BCC iron.

[1]

$$E_a = K_u \sin^2 \theta \quad (1.2)$$

Where  $\theta$  is the angle between the magnetization and the easy axis, and  $K_u$  are the anisotropy constants.  $E_a$  is a minimum when  $M_s$  is in that direction. When  $K_u$  is positive, energy is minimum at  $\theta = 0$  which is the axis of easy magnetization.

#### 1.1.4 Effect of stress on magnetic anisotropy

Magnetostriction is a property of magnetic materials that causes them to change their shape or dimensions during the process of magnetization.

If a material has positive magnetostriction coefficient ( $\lambda_l$ ), it will elongate when magnetized.

On imposing an additional strain on the sample it is expected that the direction of the magnetization will change. From our previous knowledge we know that in the absence of strain, the direction of  $M_s$  is controlled by crystal anisotropy. Therefore, when a strain is acting, the direction of  $M_s$  of the sample is controlled by both strain ( $\sigma$ ) and crystal anisotropy. So the general relation which involve both magnetisation ( $M_s$ ) and stress is given as:

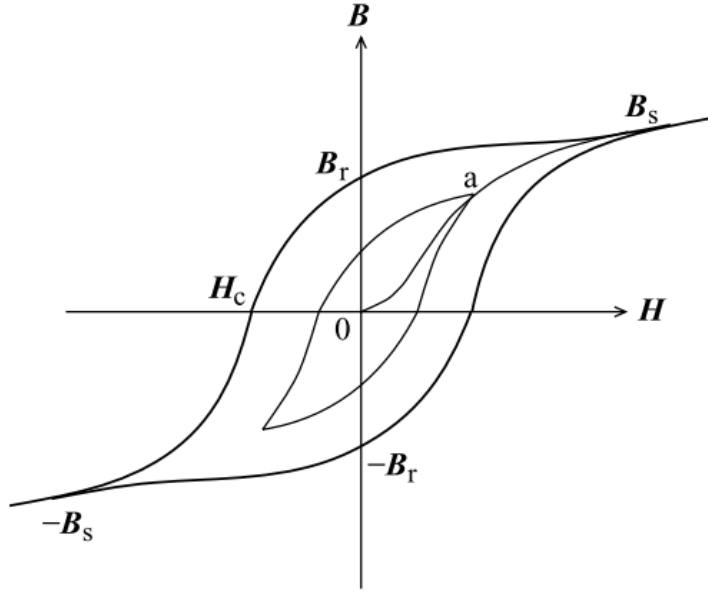


Figure 1.5: Hysteresis loop for a ferro- or ferrimagnet.  
[1]

$$E_{me} = \frac{3}{2} \lambda_{si} \sin^2 \theta \quad (1.3)$$

where  $\theta$  is the angle between  $M_s$  and  $\sigma$ .

This relation can show how a material responds to a applied stress depends only by the sign of the product of  $\lambda_{si}$  and  $\sigma$ ; of a material.

### 1.1.5 Hysteresis

The phenomenon in which the magnetic induction ( $B$ ) lags behind with respect to the magnetizing field ( $H$ ) is called hysteresis. It occurs when an external magnetic field is applied to a ferromagnet such as iron and the atomic dipoles align themselves with it. Even when the field is removed, part of the alignment will be retained: the material has become magnetized. Once magnetized, the magnet will stay magnetized indefinitely.

#### Retentivity

The property of the magnetic material to retain magnetism even in the absence of the magnetizing field is known as retentivity or remanence. Figure 1.5  $B_r$  represents the remanence field.

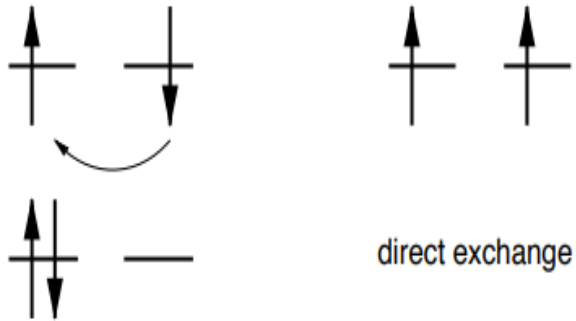


Figure 1.6: Direct exchange mechanism: The antiparallel alignment of the spins (left) is favored, since it allows the electrons to hop to the neighboring site. For parallel spins (right) hopping is suppressed by the Pauli exclusion principle.

### Coercivity

The magnetizing field ( $H$ ) needed to demagnetize the magnetic material completely is known as its coercivity. Figure 1.5  $\mathbf{H}_c$  represents the coercive field.

## 1.2 Exchange interactions

The interactions among magnetic moments as well as the interactions between magnetic moment and external magnetic field include the Heisenberg exchange interaction, DMI, magnetic anisotropy interaction, Zeeman interaction, and dipole-dipole interaction [2].

### 1.2.1 Heisenberg exchange

A strong but short-range effect, where only the nearest-neighbor (NN) sites are taken into account usually. According to the Heisenberg exchange model, the energy between neighboring spins,  $\mathbf{S}_i$  and  $\mathbf{S}_j$  can be written as[2]:

$$H_{\text{Heis}} = -J_{ij} \sum_{i,j} < \mathbf{S}_i \cdot \mathbf{S}_j > \quad (1.4)$$

where  $J_{ij}$  is the exchange constant between  $\mathbf{S}_i$  and  $\mathbf{S}_j$ .

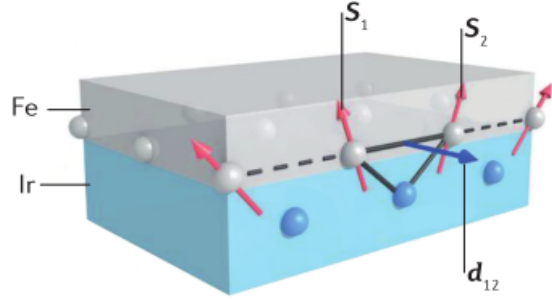


Figure 1.7: Dzyaloshinskii–Moriya interactions. Schematic picture illustrating the Dzyaloshinskii–Moriya interaction (DMI) at the interface between a magnetic film and a heavy metal. The DMI is mediated by electrons that interact by an exchange mechanism with the spins of the atoms in the magnetic layer, and that have spin–orbit coupling to the heavy metal sites.  $\mathbf{S}_1$  and  $\mathbf{S}_2$  label the spins of neighbouring atoms, and  $\mathbf{d}_{12}$  is the corresponding Dzyaloshinskii–Moriya vector.[4]

### 1.2.2 Dzyaloshinskii-Moriya Interaction (DMI):

An antisymmetric exchange interaction, which arises from the spin-orbit coupling [3]. It occurs at the interface between a magnetic thin film layer and a heavy-metal layer with strong spin-orbit coupling and also in the bulk materials lacking inversion symmetry[2].

$$H_{DMI} = (\mathbf{S}_1 \times \mathbf{S}_2) \cdot \mathbf{d}_{12} \quad (1.5)$$

### 1.2.3 Anisotropy:

The energy costs to turn the magnetization from the direction of easy axis into any other direction. In the framework of micromagnetics, the average energy density of the uniaxial magnetic anisotropy is given by[2]:

$$E_{ani} = -\mathbf{K}(\mathbf{m} \cdot \mathbf{n})^2 \quad (1.6)$$

where  $\mathbf{K}$  is the anisotropy constant, and  $\mathbf{n}$  is the easy axis.

### 1.2.4 Zeeman energy:

The Zeeman interaction tends to turn the magnetization to the same direction as the applied magnetic field, it is expressed as[2]:

$$E_{Zeeman} = -\mu_0 \int_V (\mathbf{M} \cdot \mathbf{H}_{\text{ext}}) dV \quad (1.7)$$

where  $\mathbf{H}_{\text{Ext}}$  is the external field,  $\mathbf{M}$  the local magnetization and the integral is done over the volume of the body.

### 1.2.5 Dipole-Dipole interaction

A long-range interaction in which magnetic dipoles generate the demagnetization field  $\mathbf{H}_d$ , with tendency to act on the moment so as to reduce the total magnetic moment. For the continuous model, the average energy density of the dipole-dipole interaction can be regarded as the Zeeman energy density of the demagnetization field, given as[2]:

$$E_{\text{dipole-dipole}} = -\frac{\mu_0}{2} (\mathbf{M} \cdot \mathbf{H}_{\text{dipole-dipole}}) \quad (1.8)$$

where the factor  $\frac{1}{2}$  is included to avoid double counting.

### 1.2.6 Ruderman–Kittel–Kasuya–Yosida (RKKY) interaction

This indirect interaction is the result of the spin polarization of conduction electrons produced by the exchange interaction of the localized moments with conduction electrons where the distance between two localized moments controls the strength of their effective exchange. The oscillatory Ruderman-Kittel-Kasuya-Yosida (RKKY) interaction of the localized magnetic moments in a metal has always played an important role in revealing the nature of the magnetic interaction in metals with partially unfilled  $d$  and  $f$  electron shells.[5]

The RKKY interaction which describes the interaction between two local impurity spins at the positions  $i$  and  $j$  in the form of an XXZ-type effective exchange Hamiltonian[5].

$$\mathcal{H}_{\text{RKKY}}^{ij} = J_x^{ij} (S_i^x S_j^x + S_i^y S_j^y) + J_z^{ij} S_i^z S_j^z \quad (1.9)$$

## 1.3 Magnetization dynamics

When a ferromagnetic material is kept in an external magnetic field the magnetic moments get aligned themselves along the external magnetic field.

If we look closely at the physics during this application of external magnetic fields, we know that the torque acting onto a magnetic moment  $\vec{\mu}$  in a magnetic field  $\vec{B}$  is  $\vec{\tau} = \vec{\mu} \times \vec{B}$

Now as torque is described as the change in angular momentum ( $\vec{L}$ ), therefore  $\vec{\tau} = d\vec{L}/dt = \vec{\mu} \times \vec{B}$ . However magnetic moment is proportional to the angular momentum in terms of the gyromagnetic ratio:  $\vec{\mu} = \gamma \vec{L}$ . Thus, equation of a magnetic moment in a magnetic field can be described as:

$$d\vec{\mu}/dt = \gamma[\vec{\mu} \times \vec{B}] \quad (1.10)$$

Solving this equation when magnetic field is applied along the z direction, we get:

$$\begin{aligned}\mu_x(t) &= C_1 \cos(\gamma B_z t) \\ \mu_y(t) &= C_2 \sin(\gamma B_z t) \\ \mu_z(t) &= C_3\end{aligned}$$

This solution describes the precession of a magnetic moment around the z-component of a magnetic field  $\vec{B}$  with the Larmor frequency  $\omega = \gamma B_z$ .

### 1.3.1 Landau-Lifshitz-Gilbert equation

In real systems the precession must relax in time towards the direction of the magnetic field, where the energy is minimum. The precessional torque is perpendicular to the magnetic field  $\vec{B}$ . Therefore there must be an additional damping torque  $\vec{\tau}_D$  perpendicular to the precessional torque  $\vec{\tau}$  and magnetization  $\vec{\mu}$ , which was introduced phenomenologically as :

$$\vec{\tau}_D = C \cdot \vec{\mu} \times d\vec{\mu}/dt \quad (1.11)$$

Where  $C = \alpha/\mu$  is a proportionality constant normalized to the magnitude of the magnetic moment. The equation of motion for  $\vec{\mu}$  then becomes:

$$d\vec{\mu}/dt = \gamma[\vec{\mu} \times \vec{B}] + C \cdot \vec{\mu} \times d\vec{\mu}/dt \quad (1.12)$$

The above equation is known as the Landau-Lifshitz-Gilbert equation, which describes the precessional motion of  $\vec{\mu}$  with the damping parameter  $\alpha$ . Now as we know we can replace the  $\vec{\mu}$  with the total magnetization  $\vec{M} = N\vec{\mu}/V$ . Therefore for the total magnetization :

$$d\vec{\mu}/dt = \gamma[\vec{\mu} \times \vec{B}] + \frac{\alpha}{M} \cdot \vec{M} \times d\vec{M}/dt \quad (1.13)$$

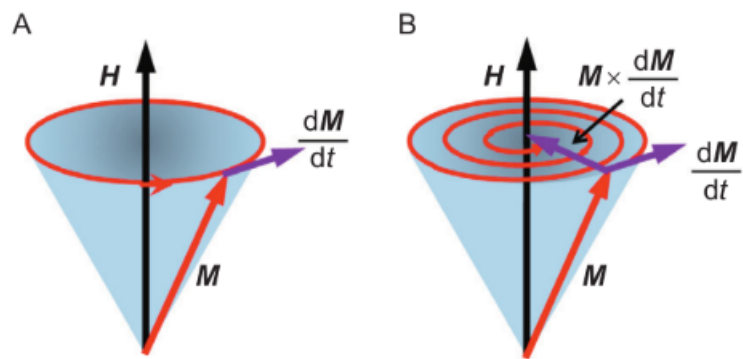


Figure 1.8: Precession of magnetization vector ( $\vec{M}$ ) around magnetic field ( $\vec{H}$ ) (A) in absence of damping term and (B) in presence of damping term

# Chapter 2

## Laser induced magnetization dynamics

### 2.1 Ultrafast demagnetization

When a femtosecond (fs) laser pulse falls on a ferromagnetic (FM) sample there is a partial or complete loss of magnetization within sub hundreds of femtoseconds this phenomena is known as ultrafast demagnetization.

The whole of event of ultrashort laser pulse interaction with the FM sample can be understood via figure 2.1. Where region 1 shows the ultrafast demagnetization followed by region 2 which shows fast remagnetization and the last is region 3 which show slow remagnetization via damped oscillations.

During the interaction total energy of the laser pulse gets transferred to the FM layer, the electrons in the FM layer get excited and reach upto a temperature of  $10^3 K$  and during this process the electrons can no longer retain their phase information of their electronic wavefunction and this results into demagnetization.

The effect was first observed by Beaurepire et al. in 1996. After this fast demagnetization process there occurs a fast recovery of the magnetization within sub-picosecond to few picoseconds and a slower recovery within tens to hundreds of picoseconds, known as the fast and slow remagnetization. Further the slower recovery is accompanied by a coherent magnetization precession and damping.

Right after the zero-delay and the interaction of the pump pulse with the electrons in the ferromagnetic metal, ultrafast demagnetization takes place. The local magnetization is immediately quenched within first few hundreds

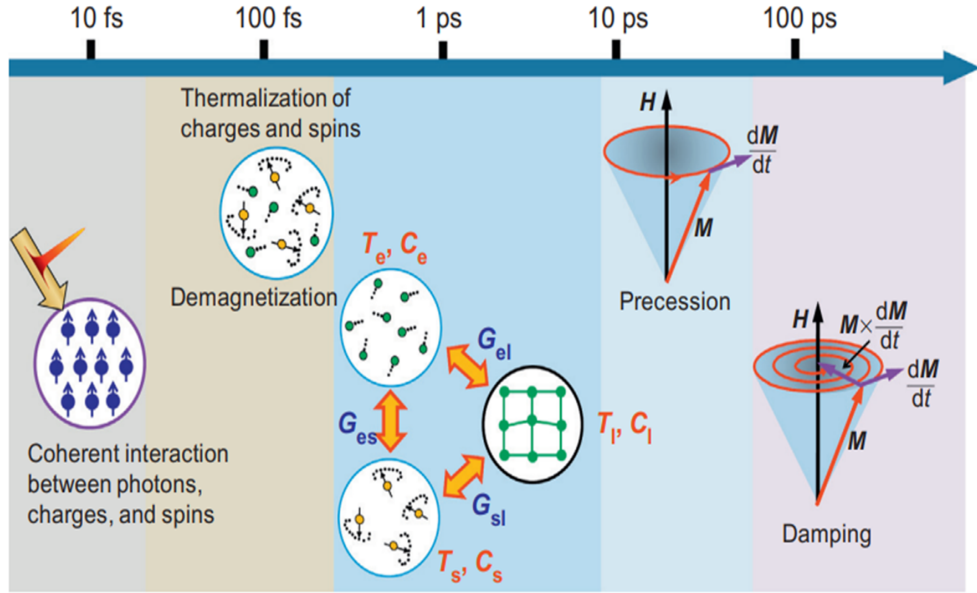


Figure 2.1: The schematic diagram of sequence of mechanisms in ultrafast magnetization dynamics.[6]

of fs followed by a subsequent fast remagnetization in next few ps. Several models have been proposed over two decades to explain the ultrafast demagnetization. Out of those the most widely accepted is a phenomenological thermodynamic model, called three temperature model, in this model the system is considered as to be made of three heat reservoirs, i.e. electron, spin and lattice. Due to the pump fluence the temperature of the electron reservoir rises almost instantly and thereafter the energy of the pump pulse is redistributed among the three different heat reservoirs as a result the spin systems temperature increases and the system becomes demagnetized. The energy exchange between the three heat reservoirs is explained using three coupled differential equation which is known as three temperature model. The coupled equations are as following:

$$C_e(T_e)dT_e/dt = -G_{el}(T_e - T_l) - G_{es}(T_e - T_s) + P(t) \quad (2.1)$$

$$C_l(T_l)dT_l/dt = -G_{el}(T_l - T_e) - G_{sl}(T_l - T_s) \quad (2.2)$$

$$C_s(T_s)dT_s/dt = -G_{es}(T_s - T_e) - G_{sl}(T_s - T_l) \quad (2.3)$$

where C are the heat capacities of the three systems, G are the coupling

constants between them, and  $P(t)$  represents the excitation from the laser pump pulse.

Neglecting electron thermalization ( $T_e$  raises instantaneously), considering  $C_6$  and  $C_p$  constant (valid in the limit of low fluence) and neglecting the spins, one obtains a 2TM that can be solved analytically:

$$\begin{aligned} C_e dT_e/dt &= -G_{el}(T_e(t) - T_l(t)) \\ C_l dT_l/dt &= -G_{el}(T_l(t) - T_e(t)) \end{aligned}$$

The solution of the above coupled differential equations can be written as:

$$\begin{aligned} T_e(t) &= T_1 + (T_{2,e} - T_1) e^{-t/\tau_E} \\ T_l(t) &= T_1 (1 - e^{-t/\tau_E}) \end{aligned}$$

Now we introduce the spin dynamics with the following rate equation:

$$dT_s(t)/dt = (T_e(t) - T_s(t))/\tau_{M,e} + (T_l(t) - T_s(t))/\tau_{M,p}$$

where  $\tau_{M,e}$  and  $\tau_{M,p}$  represent the contribution to the demagnetization time from the electron-spin channel and the phonon-spin channel. Then we obtain the general analytical solution for the spin temperature:

$$T_s(t) = T_1 - \frac{(\tau_E T_2 - \tau_M T_1) e^{-t/\tau_M} + \tau_E (T_1 - T_2) e^{-t/\tau_E}}{(\tau_E - \tau_M)}$$

where  $T_2$  is defined as  $T_{2,e} (\tau_M/\tau_{M,e})$  and  $1/\tau_M = 1/\tau_{M,e} + 1/\tau_{M,p}$ . Note that the result shows that an overall  $\tau_M$  (including both contributions via the s-p and s-e channel) can be fitted, without prior knowledge of which of the two channels dominates, and without needing information from transient reflection.

The fitting function is easily derived. First we assume a linear relation between magnetization and temperature (i.e. we linearize the  $M_s$  vs.  $T$  curve, which is justified at low fluence) thus converting the temperatures  $T_1$  and  $T_2$  into the constants  $A_1$  and  $A_2$ , respectively. We then introduce the term  $F(\tau_0, t)$  to properly take into account heat diffusion, and we add the term  $A_3\delta(t)$  to describe the effect of optical artifacts. Finally, convolution with the Gaussian laser pulse gives the following:

$$-\Delta M_z(t)/M_{0,z} = \left[ \left( A_1 F(\tau_0, t) - \frac{(A_2 \tau_E - A_1 \tau_M) e^{-t/\tau_M}}{\tau_E - \tau_M} - \frac{\tau_E (A_1 - A_2) e^{-t/\tau_E}}{\tau_E - \tau_M} \right) \Theta(t) + A_3 \delta(t) \right] * \Gamma(t) \quad (2.4)$$

[7]

### 2.1.1 Elliot-Yafet (EY) scattering

Immediately after the discovery of ultrafast demagnetization, a plethora of theoretical and experimental works were reported investigating the mechanism responsible for this novel phenomenon. Among those, application of Elliot-Yafet (EY) scattering mechanism gained huge interest. In 2005, Koopmans et al. tried to find correlation between the ultrafast demagnetization and Gilbert damping. Their work was based on the scattering mechanism proposed much earlier by Elliot and Yafet which considers the scattering between the electron and the impurity or phonon present in the system just after the arrival of pump pulse. These processes were facilitated by the SOC which transfers angular momentum between electron and lattice. Before excitation, the electron and spin baths remain in equilibrium. Immediately after the excitation, the electronic system goes into nonequilibrium but the spin system remains unchanged. Once the phonon takes away the angular momentum from the electron, the demagnetization takes place mediated by the flipping of uncompensated spins. Later, researcher tried to find the reason behind the fast demagnetization of transition metals (TM) and their alloys and slow demagnetization of rare earth (RE) metals. A compact differential equation based on EY scattering was used to describe the ultrafast magnetization dynamics:

$$\frac{dm}{dt} = Rm \frac{T_p}{T_c} \left[ 1 - \coth \left( \frac{mT_c}{T_e} \right) \right] \quad (2.5)$$

$$R \propto a_{sf} \frac{T_c^2}{\mu_{atomic}} \quad (2.6)$$

where  $a_{sf}$  is the spin-flip probability and if it increases then demagnetization will be faster (e.g.  $a_{sf}$  is larger for Co, Ni but smaller for Gd).  $R$  is a material-specific scaling factor for the demagnetization rate. It was predicted that if the demagnetization is governed by thermalization of electron then with increasing excitation energy demagnetization time would have decreased, which is not the real situation. In the pump-probe experiments, total number of involved photon is less, thus non-thermal processes was thought to be not responsible for ultrafast demagnetization.

### 2.1.2 Coulomb scattering (EY-like mechanism without considering phonon bath)

M. Krau et al. demonstrated the underlying mechanism of ultrafast demagnetization in ferromagnetic materials due to an EY-like mechanism which is

based on electronelectron Coulomb scattering. This scattering mechanism is not of quasi-elastic type. This indicates that the available phase space for transitions from the minority to the majority bands is greater than for electron-phonon scattering. The electronic distributions in the ferromagnet before excitation are assumed to be Fermi-Dirac distributions governed by the lattice temperature and band structure. The minority and majority energy dispersions are spin split resulting in a nonzero magnetization at equilibrium. Nonequilibrium electronic distributions in the bands are created due to the ultrafast optical excitation process. Deposition of energy by the pump photon forces the electrons to undergo intraband as well as interband Coulomb scattering. Assumptions about the dipole matrix elements reveal the optical excitation process cannot modify the magnetization. Thus, ultrafast demagnetization takes place when interband scattering processes between the optically energized electrons results in the repopulation of electrons from the majority to the minority bands. The fast remagnetization occurs due to energy transfer to the lattice bath.

### 2.1.3 Magnetization precession

Beside ultrafast demagnetization, the other laser-induced phenomenon that occurs right after the heating of the laser pulse is magnetization precession. This can be triggered via a perturbation of the effective field  $H_{eff}$  determining the equilibrium magnetization direction.  $H_{eff}$  usually results from the action of externally applied fields and internal anisotropies. Laser heating can induce a perturbation of these anisotropies on a sub-ps timescale in particular experimental geometries. The magnetization precession is described by the Landau-Lifshitz-Gilbert (LLG) equation as we have discussed earlier. In this project, the important aspect of magnetic damping in ferromagnetic/nonmagnetic (FM/NM) bilayer films is presented. Before describing experimental findings, we discuss two important mechanisms involved in FM/NM bilayer system, namely spin pumping and interfacial d-d hybridization.

### Spin Pumping

Ultrafast demagnetization of magnetic layers pumped by a femtosecond laser pulse is accompanied by a nonthermal spin-polarized current of hot electrons. It is possible that there is not just a single physical mechanism responsible for the laser induced demagnetization and that the contributions of the various mechanisms would depend on which materials are involved. The theoretical description of Battiato, Carva, and Oppeneer proposes that the loss of

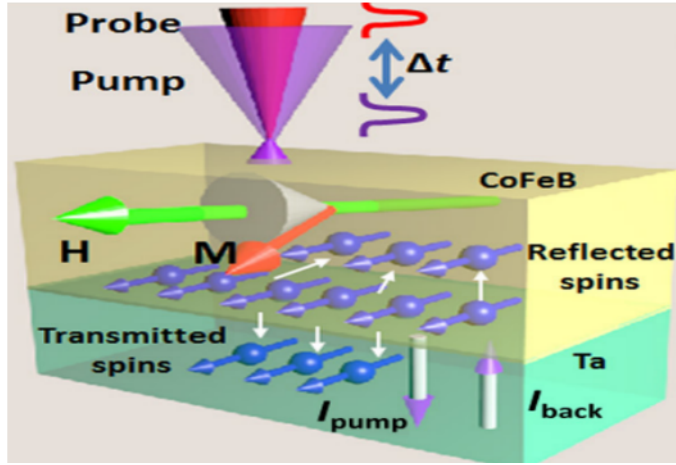


Figure 2.2: Schematic of spin pumping phenomena.[8]

magnetic moment in a magnetic layer after the laser irradiation is caused by the transport of the laser-excited electrons into adjacent metallic layers or substrate. The asymmetry of the transport properties with respect to the electron spin orientation in magnetic materials then leads effectively to a superdiffusive spin current (SC). This non-equilibrium SC not only reduces the magnetization of the pumped layer, but has also been shown experimentally to affect adjacent magnetic layers or to generate THz spin-current pulses. Notably, spin currents represent a key component of spintronics, and control over femtosecond SCs is highly desirable for potential spintronic applications operating at THz frequencies.

The laser pulses applied to a magnetic layer provide ultrashort spin current pulses on the timescale of the demagnetization – femtoseconds. In the case of laser-excited spin current the energy distribution is more complex. Here the non-thermal electrons are located at energies of about one eV above the Fermi level after being first excited from the d band to the sp band. Since the electron mobility in the sp band is much larger than that in the d band, the current that is perpendicular to both the magnetization and the chemical potential in the non-magnet. Interestingly, both of these components are absorbed at the interface giving rise to a torque on the magnetization. Furthermore, due to spin filtering and dephasing, the sum over the reflection amplitudes vanishes. Particularly, in case of transition metals, the real part of the mixing conductance is roughly proportional to the number of conducting channels, and the imaginary part is close to zero.

## Interfacial d-d Hybridization

Among various microscopic theories of Gilbert damping, Kambersky's model developed in 1976 suggests that the Gilbert damping originates from spin-orbit scattering of band electrons in ferromagnetic metals. A crude approximation for damping within this model yields following expression:

$$\alpha \approx \frac{1}{\gamma M_s} \left[ \frac{\mu_B^2 D(E_F)}{\tau_E} \right] \left( \frac{\xi}{W} \right)^2 \quad (2.7)$$

where  $D(E_F)$  is the density of states at the Fermi level for d-bands,  $M_s$  is the saturation magnetization,  $\mu_B$  is Bohr magneton,  $\tau_E$  is the electron momentum relaxation time,  $\xi$  is the spin-orbit coupling parameter, and  $W$  is the typical band width of d-bands. Though the mechanism of d-d hybridization has been invoked in several experimental studies in order to explain the enhanced value of damping, the detailed theoretical study for d-d hybridization in the context of its implication on Gilbert damping is limited to few studies. Most theoretical and experimental studies regarding d-d hybridization have been related to the explanation of perpendicular magnetic anisotropy (PMA) in the FM/NM systems. There have been further attempts to provide a generic overview on the correlation of PMA with the damping; however, up to date, there has not been a clear understanding due to variation in results obtained for different samples and interpretation provided by various research groups.

# Chapter 3

## Spin and Spin Current

The quantum mechanical property of fundamental particles, namely ‘spin’ is well known. The mental picture depicts that ‘spin’ represents angular momentum associated with the particle during spinning about its own axis. However, this classical picture is inadequate and oversimplified to describe the quantum mechanical property.

### 3.1 Spin Polarization

In quantum mechanics ‘spin’ can be expressed as an operator:

$$\hat{s} = \frac{\hbar}{2}\hat{v} \quad (3.1)$$

where  $\hat{\sigma}$  is the Pauli spin matrix given by:

$$\hat{\sigma}_x = \begin{pmatrix} 0 & 1 \\ 1 & 0 \end{pmatrix} \quad \hat{\sigma}_y = \begin{pmatrix} 0 & -i \\ i & 0 \end{pmatrix} \quad \hat{\sigma}_z = \begin{pmatrix} 1 & 0 \\ 0 & -1 \end{pmatrix} \quad (3.2)$$

The wave function related to spin degree of freedom can be written as:

$$\psi(r, t) = a|\uparrow\rangle + b|\downarrow\rangle = \begin{pmatrix} a \\ b \end{pmatrix} \quad (3.3)$$

The probability density is:

$$\rho(r, t) = \psi^\dagger(r, t)\psi(r, t) \quad (3.4)$$

and spin density as:

$$\rho_s(r, t) = \psi^\dagger(r, t)s\psi(r, t) \quad (3.5)$$

In terms of spinors, the spin charge can be described as below,

$$s(r, t) = \frac{\rho_s(r, t)}{\rho(r, t)} = \varphi^\dagger \hat{S} \varphi \quad (3.6)$$

$$s(r, t) = \frac{\rho_s(r, t)}{\rho(r, t)} = \frac{\hbar}{2} \varphi^\dagger \hat{\sigma} \varphi = \frac{\hbar}{2} p(r, t) \quad (3.7)$$

The polarization vector ( $\mathbf{p}$ ) of a spin charge of electron is a real pseudovector in threedimensional space. For an entire ensemble if the majority of spin belong to a particular state, then the beam is polarized. On the other if they are equally distributed within the states then it is unpolarized.

## 3.2 Spin Current

Now suppose in a system carrier density is  $n$  and probability densities for up and down states are  $a_2$  and  $b_2$ , then the charge density and spin density become,

$$\rho_c = -e(a^2 + b^2) \quad (3.8)$$

$$\rho_s = \frac{\hbar}{2}(a^2 - b^2) \quad (3.9)$$

$$a^2 = n_\uparrow, b^2 = n_\downarrow, a^2 + b^2 = n \quad (3.10)$$

where  $n$  is the total number of elements. Thus, if the current densities of each spin states can be described by:

$J_{\uparrow(\downarrow)} = en_{\uparrow(\downarrow)}v$  Charge current density and spin current density will be,

$$J_c = \rho_c v = J_\uparrow + J_\downarrow \quad (3.11)$$

$$J_s = \rho_s v = \frac{\hbar}{2c}(J_\uparrow - J_\downarrow) \quad (3.12)$$

The units of charge current and spin current are not the same. In SI system the unit of charge current is  $A/m^2$ . The unit of spin current is  $\frac{\hbar}{e} A$ . When spins with opposite polarity get deflected in two opposite directions then the resultant spin imbalance is known as ‘spin current’. This spin current can be categorized in to four different kinds: pure spin current, partially spin polarized current, fully spin polarized current and unpolarized current as shown in Figure 3.1.

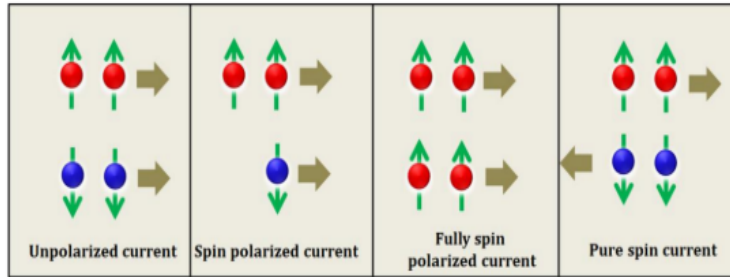


Figure 3.1: Variety of spin current: Unpolarized current, spin polarized current and pure spin current

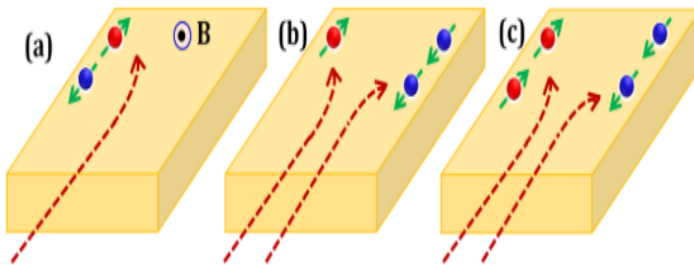


Figure 3.2: Hall geometries: (a) ordinary Hall effect, (b) anomalous Hall effect and (c) spin Hall effect.

### 3.3 Hall effect

E. Hall discovered this effect in 1879. This effect describes that if charge current is applied in a material in presence of a transverse magnetic field, an electric field is developed within the material perpendicular to both the applied fields. There are varieties of Hall effect as shown in Figure 3.2:

#### 3.3.1 Ordinary hall effect

An example can describe this effect better. For a simple metal with only one type of charge carrier (i.e. electrons), the Hall voltage ( $V_H$ ) can be estimated by using the Lorentz force. A piece of metal having dimension  $L \times b \times d$ , is placed in magnetic field  $B_y$ . If charge current (of electric field E) is applied along x direction then the Lorentz force acting upon the electrons is:

$$\vec{F} = e(\vec{E} + \vec{v} \times \vec{B}) \quad (3.13)$$

Now accumulation of charge in the top and bottom surface will generate

a Hall voltage,

$$V_H = z \cdot E_H = e(v \times B) = \frac{IB}{ne} \quad (3.14)$$

Where  $I = ne\vec{v}bd$ ,  $n$  is number of particle,  $\vec{v}$  is velocity and other symbols have usual meaning. If  $\vec{j}$  is considered as applied charge current density then the Hall coefficient can be expressed as,

$$R_H = \frac{E_H}{jB} \quad (3.15)$$

In SI units it becomes,  $R_H = -\frac{1}{ne}$

### 3.3.2 Anomalous Hall effect

In ferromagnetic system additional contribution to Hall voltage comes from the anomalous Hall effect (AHE). Here, presence of external magnetic field is not required. Due to the application of charge current spin dependent scattering leads to deviation of electrons with opposite spin polarity in opposite directions. Since the material is ferromagnet it has difference in majority and minority spin population in the bands. Thus, the number of electrons with either kinds of spin polarity accumulated after deviation will be larger than the other. This will create an additional charge imbalance, which is proportional to the magnetization of the material and is different from ordinary Hall effect. The total Hall resistance then in the material will have two contributions:  $R_H = R_0B + R_AM$ . Here  $R_0$  and  $R_A$  are the ordinary and anomalous Hall coefficients. The AHE is of two types, i.e. intrinsic and extrinsic effects. It is worth to mention here that quantized version of intrinsic AHE is known as quantum Hall effect (QHE).

### 3.3.3 Spin Hall effect

In presence of charge current in some of the materials, the spins with opposite polarity get deflected in two opposite directions creating a spin imbalance. Without application of any external magnetic field this spin imbalance originates a spin current ( $J_s$ ). This phenomenon is known as spin Hall effect. As this current is transverse to the applied electric field  $\vec{E}$ , then  $\vec{J}_s \cdot \vec{E} = 0$ . There is no Joule heating associated with pure spin current as the net amount of accumulated electrons are same in either side of the material surface. There are two types of spin Hall effect: intrinsic effect is caused by Rashba spin-orbit interaction. The extrinsic effect arises from the spin dependent scattering.

There are two explicit mechanisms responsible for the occurrence of extrinsic spin Hall effect:

### **Skew scattering mechanism**

N. F. Mott in 1929 suggested that polarized electron scatters asymmetrically due to SO coupling. When an itinerant electron passes through the vicinity of electric field produced by impurity or scattering centers,  $\vec{B} = \vec{v} \times \vec{E}$  is felt by the electron in its own frame perpendicular to the scattering plane. Now  $\vec{B}$  is inhomogeneous over space and sign changes when the electron with different polarity deflects from different sides of the impurity. The force of deflection due to Zeeman effect depends on polarity of spin.

### **Side jump mechanism**

When SOC is acting on a system the symmetry is low. Hence a travelling electron not necessarily retains a straight line path and either deflects with an angle  $\theta$  or shifts with a path  $\Delta y$  after scattering. This mechanism has purely quantum mechanical nature. An anomalous velocity  $\vec{v}$  of electron occurs which is spin dependent,

$$H = \frac{p^2}{2m} + eV + V_{so} \quad (3.16)$$

$H$  is Pauli Hamiltonian in presence of spin-orbit interaction.

$$V_{so} = \frac{\hbar}{4m^2c^2} (\vec{\sigma} \times \nabla \vec{v}) \cdot \vec{P} \quad (3.17)$$

$$\vec{v} = \frac{\partial \vec{H}}{\partial \vec{P}} = \frac{\vec{P}}{m} - \frac{e\hbar}{4m^2c^2} \vec{E} \times \vec{P} \quad (3.18)$$

Here  $\vec{E}$  is electric field,  $\vec{\sigma}$  is the spin polarity and  $\vec{P}$  is momentum vector.

# **Chapter 4**

## **Experimental technique**

In this project the dynamics of spins in ferromagnetic thin films down to the femtosecond timescale is studied. The main experimental tool used for this study is time-resolved magneto-optical Kerr effect (TR-MOKE). In this technique a laser pulse is divided into pump and probe pulses of femtosecond order, when the pump pulse falls on the experimental sample it perturbs the magnetization dynamics mostly by heating the sample, after that the weaker probe pulse is used to investigate the magnetization dynamics created by the pump pulse.

### **4.1 Magneto-Optical Kerr Effect (MOKE)**

The term “magneto-optics” refers to the various phenomena which occur when electromagnetic radiation interacts with magnetically polarized materials, and ”Kerr-effect” is a surface phenomena where plane of polarization of a light rotates when the light gets reflected from the magnetized sample surface.

### **4.2 Theory of magneto-optical Kerr effect**

When linearly polarised light reflects from a ferromagnetic sample placed in the external magnetic field then there is rotation in plane of polarisation of light due to which linearly polarised light becomes elliptically polarised this effect is known as magneto optical Kerr effect.

### 4.2.1 Physical Origin of Magneto-Optical Effects

The origin of magneto-optical effect can be explained by Zeeman effect. Let us consider a system of electrons bound harmonically in an oscillating electric field and a static magnetic field. The equation of motion of each electron can be written as:

$$m\ddot{r} + b\dot{r} + kr = -eE_0e^{j\omega t} - e\mu_0\dot{r} \times H \quad (4.1)$$

where  $b$  is the damping coefficient,  $k$  is the restoring force constant,  $m$  is the electron mass and  $\sqrt{(k/m)} = \omega_0$  is the natural frequency of electron. The last term in this equation is the Lorentz force. The above equation can easily be solved. The electric dipole moment ( $-er_0$ ) is proportional to the electric field ( $E_0$ ). The proportionality tensor is called the polarizability tensor. For an assembly of  $N$  oscillators the polarizability can be expressed:

$$\begin{aligned} \chi_{xx} = \chi_{yy} &= \frac{Ne^2}{\epsilon_0 m} \frac{\omega_0^2 - \omega^2 + j\omega\gamma}{(\omega_0^2 - \omega^2 + \omega\gamma)^2 - 4\omega^2\omega_L^2} \\ \chi_{xx} = \chi_{yy} &= \frac{Ne^2}{\epsilon_0 m} \frac{-2j\omega\omega_L}{(\omega_0^2 - \omega^2 + \omega\gamma)^2 - 4\omega^2\omega_L^2} \end{aligned} \quad (4.2)$$

where  $\omega L = e\mu_0 H/2m$  is the Larmor precession frequency and  $\gamma = b/m$  is the width of the resonance.  $\chi$  is a symmetric and scalar quantity in an isotropic medium.

Therefore the off-diagonal terms of the dielectric tensor are zero. The anisotropy in the medium may be generated from the magnetic field or the magnetization of the ferromagnetic material. For a circularly polarized light, the polarizability can be written as:

$$\chi_{xx} = \chi_{yy} \pm i\chi_{xy} = \frac{Ne^2}{\epsilon_0 m} \frac{\omega_0^2 - \omega^2 + j\omega\gamma \pm 2\omega\omega_L}{(\omega_0^2 - \omega^2 + j\omega\gamma)^2 - 4\omega^2\omega_L^2} = \frac{Ne^2}{\epsilon_0 m} \frac{1}{\omega_0^2 - (\omega \pm \omega_L)^2 + j\omega\gamma} \quad (4.3)$$

The upper sign refers to the right circularly polarized (RCP) light, whereas the lower sign to the left circularly polarized (LCP) light. Larmor's theorem says that if the refractive index in absence of magnetic field is  $n(\omega)$ , then in presence of a field the refractive indices can be written as:

$$n_{\pm}(\omega) = n(\omega \pm \omega_L) \quad (4.4)$$

Therefore, the refractive indices of RCP and LCP are different in presence of a magnetic field. Let us now consider a linearly polarized light propagating

in a circularly birefringent medium. Then it can be considered to be linear combination of RCP and LCP light. As the refractive index of the RCP and LCP is different so there will be a phase difference will be created between them by the birefringence of the medium. So the direction of polarization of linearly polarized light is being rotated through an angle of  $\delta/2$ . Where  $\delta$  is the phase difference created between the RCP and LCP. If the medium is absorptive then the linearly polarized light will be converted to an elliptically polarized light with the major axis of the ellipse rotated through an angle  $\delta/2$ . Ellipticity introduced is given by  $\tanh(\delta/2)$ .

#### 4.2.2 Phenomenological theory of MOKE

The optical properties of material can be given by Maxwell's equations and the corresponding relations, which describe the specific material properties. We need two equations:

$$\nabla \times H = j + \frac{\partial}{\partial t}(\epsilon_0 E + P) \quad (4.5)$$

$$\nabla \times E = -\frac{\partial B}{\partial t} \quad (4.6)$$

where  $E$ ,  $H$ ,  $j$ ,  $\epsilon_0$  are electric field, magnetic field, electrical current density and permittivity of free space, respectively. The current density can be expressed as:

$$J = \epsilon_0 \frac{\partial P}{\partial t} = \chi \frac{\partial E}{\partial t} \quad (4.7)$$

where  $\chi$  is the polarizability. Again dielectric constant ( $\kappa$ ) and polarizability ( $\chi$ ) are related by the relation:

$$\kappa = 1 + \chi \quad (4.8)$$

$\kappa$  and  $\chi$  are the tensorial quantities and depends on the applied magnetic field and magnetization of the material. Their non-scalar nature gives rise to the magneto-optical effect. Now we consider a plane propagating wave propagating through a medium. The electric and magnetic fields may be written as:

$$E = E_0 e^{j(\omega t - k \cdot r)}, H = H_0 e^{j(\omega t - k \cdot r)} \quad (4.9)$$

Taking curl of above equation will give:

$$n^2 - k \cdot \frac{k}{k_0^2 - K} \cdot E_0 = 0 \quad (4.10)$$

The eqn(4.10) posses a non-trivial solution for  $E_0$  only if the determinant of coefficient vanishes. Now if we consider a cubic crystal with DC magnetic field applied along the z-axis. Then, the dielectric constant can be given as:

$$\boldsymbol{\kappa} = \begin{bmatrix} \kappa_1 & \kappa_2 & 0 \\ -\kappa_2 & \kappa_1 & 0 \\ 0 & 0 & \kappa_3 \end{bmatrix} \quad (4.11)$$

In the above equation,  $\kappa_2$  is the odd function of  $\mathbf{H}$  or  $\mathbf{M}$ , whereas  $\kappa_1$  and  $\kappa_3$  even functions. With the above form of  $\kappa$ , the secular determinant for equation-16 becomes

$$n^4 \{k_1 + (k_3 - k_1) \cos^2 \theta'\} - n^2 \{(k_1^2 + k_2^2 + k_1 k_2) - (k_1^2 + k_2^2 - k_1 k_2) \cos \theta'\} + k_3 (k_1^2 + k_2^2) = 0 \quad (4.12)$$

where

$$\cos \theta' = k_Z / nk_0 \quad (4.13)$$

Let us now consider the simplest case. A homogeneous wave (real and imaginary part of  $\mathbf{k}$  are parallel) with propagation direction along  $H$  or  $M$ . In this case,  $\cos \theta' = 1$ . Therefore the solutions of equation-17 are

$$n_{\pm} = k_1 \pm k_2 \quad (4.14)$$

For simplicity, we now consider the polar Kerr effect at normal incidence. Let  $k_0$   $k_1$  and  $k_2$  are the incident, reflected and transmitted wave vectors, respectively. The reflected amplitude can be written as:

$$r = \frac{E_1}{E_0} = -\frac{n-1}{n+1} \quad (4.15)$$

If we write reflectivity as:

$$r = |r| e^{i\phi} \quad (4.16)$$

Then

$$\frac{r_+}{r_-} = \left| \frac{r_+}{r_-} \right| e^{i(\phi_+ - \phi_-)} \quad (4.17)$$

The above relation says that the linearly polarized light will be converted to elliptically polarized light upon reflection because the circular components

(RCP & LCP) will not have equal amplitudes. The major axis of the ellipse will be rotated from the original direction of polarization of the incident light because of the phase introduced between the two circular vibrations. The Kerr rotation and ellipticity can be expressed as:

$$\phi_k = \frac{1}{2}(\phi_+ - \phi_-) \quad (4.18)$$

$$\epsilon_k = -\frac{r_+ - r_-}{r_+ + r_-} \quad (4.19)$$

Now, expressing the refractive index as a complex quantity, the complex Kerr rotation can be written as

$$\theta_k = \frac{2}{1-\epsilon} [-(k_- - k_+) + i(n_- - n_+)] \quad (4.20)$$

The real component of  $\theta_k$  gives the Kerr rotation and imaginary component of  $\theta_k$  gives the Kerr ellipticity. The Kerr rotation depends upon the circular dichroism, whereas Kerr ellipticity depends upon the circular birefringence of the medium. It can also be shown qualitatively that the Kerr rotation and Kerr ellipticity both are proportional to the magnetization of ferromagnetic material.

### 4.3 MOKE Geometries

Depending upon the direction of magnetization vector ( $\vec{M}$ ) and plane of incidence of light the geometries can be classified into three types as Polar, Longitudinal and Transverse.

1. Polar : In polar geometry the magnetization vector is perpendicular to the sample surface and parallel to the plane of incidence of the light.
2. Longitudinal : In longitudinal geometry the magnetization vector is parallel to the sample surface and to the plane of incidence of light.
3. Transverse : In Transverse geometry the magnetization vector is parallel to the sample surface and perpendicular to the plane of incidence. Figure 4.1 shows all the MOKE geometries.

The Kerr rotation can be explained qualitatively by considering the interaction of the electric field (E) of the light with the magnetization of the material. In a linearly polarized light (let us say p-polarized light), the electrons in the sample oscillate along the E-field of the light. For a p-polarized

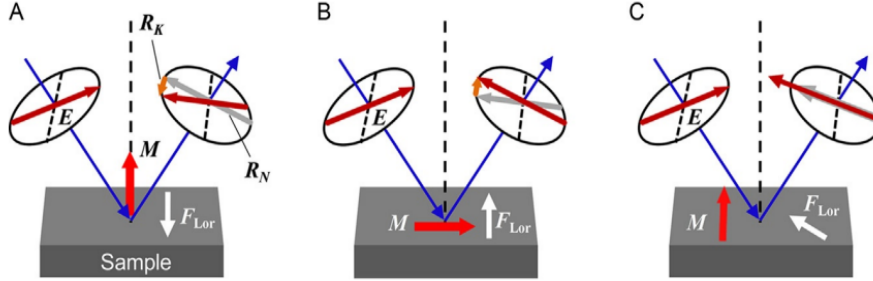


Figure 4.1: The schematic diagrams of (a) polar, (b) longitudinal, and (c) transverse MOKE are shown.

light, the oscillation is in the plane of incidence of the beam and also in the plane of the sample. Again, a regularly reflected light experiences a  $\pi$  phase change w.r.t. the incident beam. Therefore, the direction of  $E$  becomes opposite to the direction of the incident electric field. The Lorentz force ( $F_{Lor}$ ) on the oscillating electrons generates an additional small vibrational component ( $k$ ) perpendicular to the plane of incidence. The electric field of the reflected light is the vector sum of the original electric field vector ( $r$ ) and the Lorentz field vector ( $k$ ). Figure 4.1 shows that the vector sum of the reflected light i.e., the resultant electric field of reflected light is rotated due to the magnetization of the sample. S-polarized light (electric field is perpendicular to the plane of incidence) gives a similar Kerr rotation for the polar effect.

The longitudinal Kerr effect is not observed at normal incidence as the cross-product is zero. For other incident angles the longitudinal Kerr effect is observed for both p- and s-polarized lights. The Kerr rotation ( $\theta_k$ ) and ellipticity ( $\epsilon_k$ ) are related to each other by a relation:  $\theta_k + i\epsilon_k = k/r$ , in the limit  $k \ll r$ . The third MOKE geometry is called the transverse geometry where  $M$  lies in the plane of the sample, but perpendicular to the plane of incidence of light. Only P-polarized light shows transverse Kerr effect. In this case, the reflected beam remains linearly polarized without any Kerr rotation, but the amplitude is changed as magnetization vector changes sign from  $+M$  to  $-M$ .

## 4.4 Time resolved measurements

The time resolution of dynamics measurements employing standard electrical characterization techniques is limited by the maximum bandwidth of the used electrical components. The bandwidth is inversely proportional to the

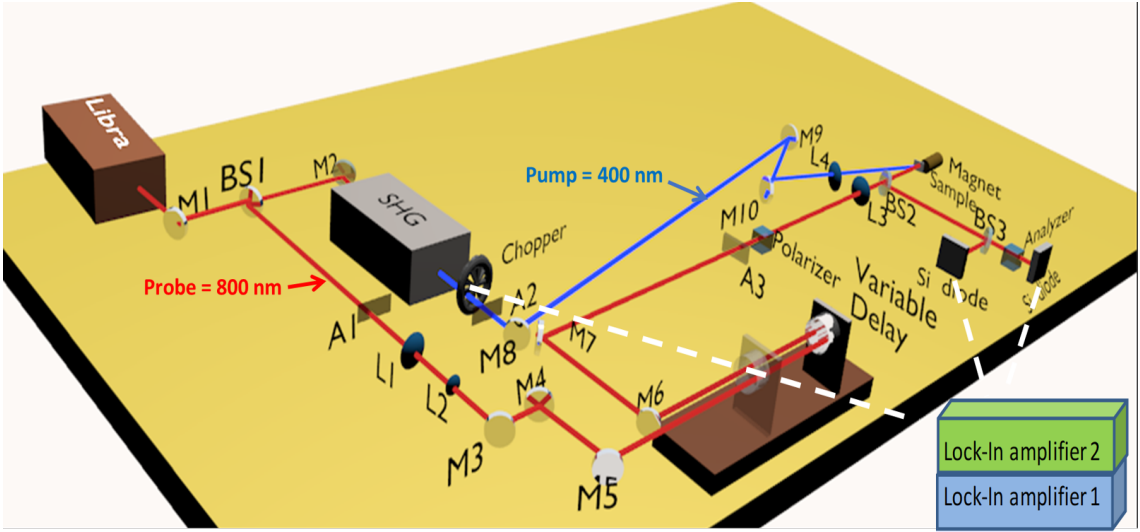


Figure 4.2: Schematic diagram of the experimental setup used to detect the TR-MOKE signal

electronic response time (RC) and the time resolution does not exceed 0.1 ns. Meanwhile, many interesting physical phenomena arise due to the interaction between lattice, electronic and spin subsystems. The timescales of these interactions range from  $10^{-18}$  s to  $10^{-9}$  s. Thus, nonelectrical methods have to be used to access the aforementioned processes in different materials.

#### 4.4.1 Ultrafast pump-probe technique

The pump-probe technique is an elegant method to dynamic measurements with a very high time resolution. The essence of this technique is to use ultra-short laser pulses with different intensities. A polarized laser beam is divided into a pump and a probe with the help of a beam splitter (BS). The high-intensity pump pulse is further used to perturb the to be investigated system out of equilibrium. The change of the initial state of a time-delayed low-intensity probe pulse (e.g. transmitted or reflected intensity, polarization) serves as the measurement tool. A time delay is set with the help of an optical delay line which is a mechanical moving stage. Changing the delay line position alters the path of the probe beam and, accordingly, its arrival time on the sample. The position of the delay line where the optical path of the probe is equal to the optical path of the pump is called "zero delay" (time zero). Measuring the pump-induced signal multiple times and averaging it for each time delay allows us to reconstruct time-resolved dynamics.

Detection is done by a photodetector and processed by a lock-in amplifier. To pick-out only the pump-induced signal, the reference channel of the lock-in amplifier is synchronized with the repetition rate of the pump pulse. In order to alter the repetition rate of the pump, a frequency modulator is installed in its path.

To measure the polarization rotation of the probe beam one utilizes a balanced detection scheme that has extremely high sensitivity to very small rotation angles. As seen in Fig., the Wollaston prism (WP) splits the incoming beam into s- and p-polarization which are detected by photodetectors A and B, respectively. When the difference between channels A and B is zero,  $A - B = 0$ , the scheme is balanced. This is achieved by rotating the optical axis of the Wollaston prism. Polarization rotation in this scheme corresponds to the signal in the difference channel  $I_A - I_B \approx \theta$ .

Let's see how this works. Let us consider a polarized beam incident on the WP with the electric field  $\mathbf{E}$  with a magnitude  $E_0$  at an angle  $\pi/4$  to the WP optical axis. The intensity measured at the channels A and B are:

$$E_A^2 = \cos^2(\pi/4)E_0^2, E_B^2 = \sin^2(\pi/4)E_0^2. \quad (4.21)$$

A slight polarization rotation of the incident beam over an angle  $\Delta\alpha$  will result in a change of the measured intensities:

$$E_A^2 = \cos^2(\pi/4 + \Delta\alpha)E_0^2, E_B^2 = \sin^2(\pi/4 + \Delta\alpha)E_0^2. \quad (4.22)$$

Thus, the intensity measured at the channel A – B equals:

$$I_A - I_B = E_A^2 - E_B^2 = E_0^2 (\cos^2(\pi/4 + \Delta\alpha) - \sin^2(\pi/4 + \Delta\alpha)) = E_0^2 \cos(\pi/2 + 2\Delta\alpha) = E_0^2 \sin(2\Delta\alpha) \quad (4.23)$$

Where  $E_0^2 = (I_A + I_B)$ . As the rotation angle  $\Delta\alpha$  becomes very small, we can see:

$$I_A - I_B \approx 2(I_A + I_B)\Delta\alpha \quad (4.24)$$

#### 4.4.2 Precessional fitting:

The precessional data can be fitted through the following equation:

$$M(t) = M(0)e^{-(t/\tau)} \sin(\omega t + \phi) \quad (4.25)$$

from the above equation relaxation time ( $\tau$ ) can be extracted.

#### 4.4.3 Effective magnetization:

The variation of  $f$  with bias magnetic field ( $H$ ) is fitted using the Kittel formula, which is given as [9]:

$$f_{fft} = \frac{\gamma}{2\pi} \left[ \left[ H + \frac{2K_2}{M_s} \cos(2\phi) - \frac{4K_4}{M_s} \cos(4\phi) \right] \times \left[ H + 4\pi M_{eff} + \frac{2K_2}{M_s} \cos^2(\phi) - \frac{K_4}{M_s} (3 + \cos(4\phi)) \right] \right]^{\frac{1}{2}} \quad (4.26)$$

On considerin the anisotropy as  $K = O$ . We get the fitting equation as:

$$f_{fft} = \frac{\gamma}{2\pi} \sqrt{H(H + 4\pi M_{eff})} \quad (4.27)$$

where,  $f_{fft}$  : frequency obtained from fft;  $\gamma$  : gyromagnetic ratio

#### 4.4.4 Effective damping:

From the Kittel fit, we estimate the effective damping,  $\alpha_{eff}$ , using the expression:

$$\alpha_{eff} = \frac{1}{\gamma\tau[H + 2\pi M_{eff}]} \quad (4.28)$$

where,  $H$  : External magnetic field,  $M_{eff}$  : Effective magnetization

# **Chapter 5**

## **Experimental setup**

### **5.1 Apparatus required**

The all optical TR-MOKE setup consists of following:

1. Laser
2. SHG
3. Attenuator
4. Chopper
5. Retro refractor (Delay stage)
6. Polarizers
7. Beam splitters
8. Reflecting mirrors
9. Focusing lens
10. Lock-in amplifier
11. Photo-diode
12. Power meter
13. IR viewer
14. Lab-view software
15. Oscilloscope
16. Chiller

### 5.1.1 Working mechanism

Before starting the experiment the chiller must be turn on and only after 4 hours when optimal base plate temperature of 18°C is reached laser must be turned on.

The S-polarized fundamental laser beam from the output of the amplifier (Libra) is guided by a set of five mirrors before being split into two equal parts using a 50:50 beam splitter (see Figure 5.1). A portion of this fundamental laser beam is fed into the SHG and after frequency doubling ( $\lambda = 400$  nm) we obtain the pump beam. The other part of the fundamental laser beam ( $\lambda = 800$  nm) is heavily attenuated and a very weak part is used as the probe beam. This beam is steered by a number of mirrors into a motorized scanning delay stage with retro-reflector (RR) for introduction of a variable time delay. Before entering into the RR the probe beam is collimated using a pair of plano-convex lenses of focal lengths 10 cm and 15 cm and its beam-waist is reduced to  $\sim 5$  mm. The probe beam coming out from the RR is guided to the sample using few mirrors before being focused on to the sample surface by using a plano-convex lens of focal length. A GT polarizer (GTH5M, Thorlabs) with extinction ratio of 100000:1, is placed in the path of the probe beam to ensure high degree of polarization of the incident probe beam. Three iris are kept in the path of the probe beam to monitor the vertical and lateral shift of the probe beam on a regular basis.

The pump beam is guided on to the sample by using a set of five mirrors which are adjusted to compensate the optical path length w.r.t. the probe path. A variable attenuator is used for adjusting the probe power falling on to the sample. The pump and probe beams are made to incident non-collinearly on to the sample surface. The pump beam is kept slightly defocused on the sample surface to avoid any damage of the sample by the high irradiation by the pump power. The probe beam is tightly focused on the sample surface and placed carefully at the centre of the pump beam so that the dynamics is probed from the uniformly excited part of the sample. The pump and probe beam have spot sizes of  $200 \mu\text{m}$  and  $100 \mu\text{m}$ . The sample is mounted on a holder placed on the top of a translational x-y-z stage. A viewing arrangement is made using a white light source and a CCD camera for monitoring the overlap of the pump and probe beams as well as their locations on the sample surface. The pump beam is blocked after reflection. The reflected probe beam is split into two parts with a beam splitter. One part is fed directly into a Si detector which measures the total reflectivity. The other part is fed into another GT polarizer (analyzer) and a Si detector, which measures the Kerr rotation of the probe beam. The analyzer is set at a very small from the extinction so that it measures the Kerr rotation on a mini-

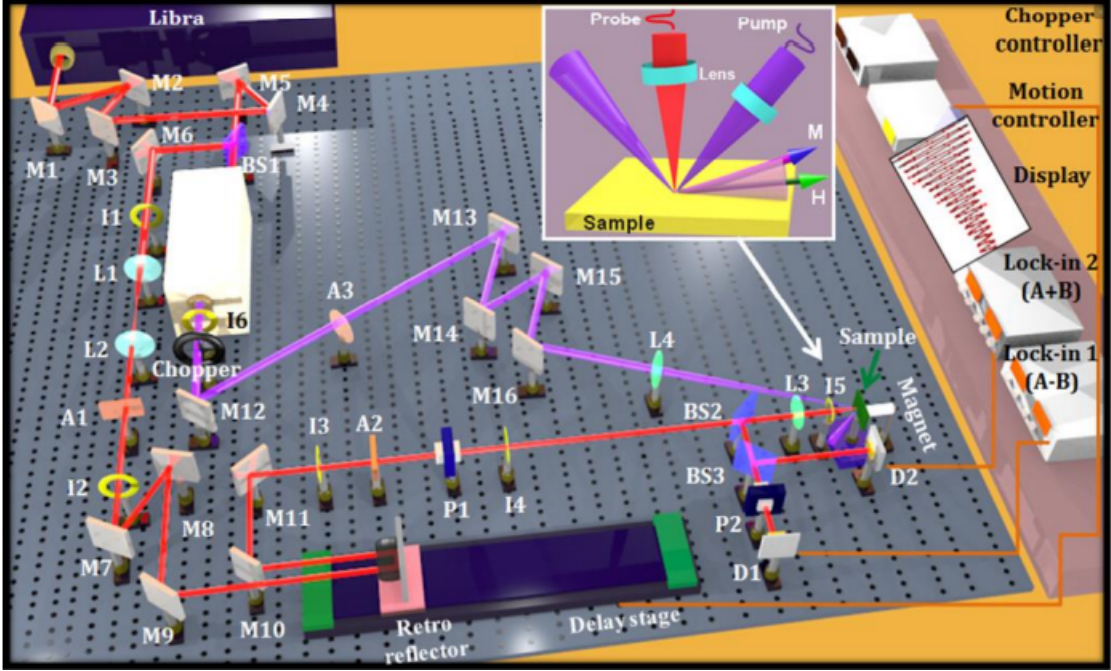


Figure 5.1: Schematic diagram of the optical pump-probe setup with amplified fs laser unit. The experimental geometry is shown in the inset.

mal background of reflectivity. The bias magnetic field is applied by using permanent magnets in the desired configuration.

It is to be noted that the pump beam incidents obliquely on the sample surface whereas the probe beam incidents normally and during the experiment only the probe path is disturbed the pump path is kept unaltered.

## 5.2 Sample details and fabrication

The ferromagnetic sample which has been studied is a ferromagnetic alloy (CoFeB) Si/SiO<sub>2</sub> (700nm)/Co<sub>20</sub>Fe<sub>60</sub>B<sub>20</sub>(5nm)/MgO(2nm)/Al<sub>2</sub>O<sub>3</sub> (10 nm) and a bilayer sytem of Si/SiO<sub>2</sub> (700nm)/Pt(10nm)/Co<sub>20</sub>Fe<sub>60</sub>B<sub>20</sub> (5nm)/MgO(2nm)/Al<sub>2</sub>O<sub>3</sub>(10 nm). The sample has been made using an RF/DC magnetron sputtering unit.

### 5.2.1 RF and DC Magnetron Sputtering System

Sputtering is based on the principle that particle to particle collisions will involve an elastic transfer of momentum which can be utilized to deposit a

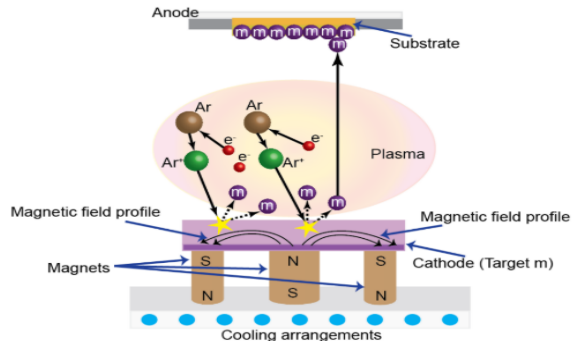


Figure 5.2: Schematic of sputtering at molecular level

thin film on a substrate. In this technique, ions are accelerated toward a target by using an electric field. These ions are usually derived from either an ion gun or from exciting a neutral gas into ion plasma. As the ions are accelerated and bombarded on the target surface, they dislodge target atoms and other ions. The ejected atoms attach themselves to the substrate and a thin film of the target material is produced. Depending on the target material either RF or DC sputtering is used. If the target material is a conductor, a constant voltage can be used to accelerate the ions to the desired bombarding velocity. As the ions strike the surface, the resulting charges can move freely about the material to prevent any charge build up. However, if the material is an insulator the conduction bands will not allow free charge movement. As the ions strike the surface, their charge will remain localized and over the time the charge will build up, making it impossible to further bombard the surface. In order to prevent this, alternating current is used at a frequency above 50 kHz. A high frequency is used so that the heavy ions cannot follow the switching fast enough and only electrons hit the surface to neutralize charge.

The multilayered stacks for this study were deposited on S(001)/SiO<sub>2</sub>(700 nm) substrates by radio frequency (RF) sputtering at room temperature at a base pressure of  $\approx 10^{-8}$  Torr. The multilayered stacks consisted of the following layers from bottom: Si/SiO<sub>2</sub>(700)/Pt(10)/Co<sub>20</sub>Fe<sub>60</sub>B<sub>20</sub>(5)/MgO(2)/Al<sub>2</sub>O<sub>3</sub>(10), where the numbers in parentheses are the nominal thicknesses of corresponding layers in nanometers and NM stands for non-magnetic materials such as Cu, Ta, W, Pt.

Two reference multilayered stacks:

Si/SiO<sub>2</sub>(700)/Pt(10)/Co<sub>20</sub>Fe<sub>60</sub>B<sub>20</sub>(5)/MgO(2)/Al<sub>2</sub>O<sub>3</sub>(10) and

$\text{Si/SiO}_2(700)/\text{Co}_{20}\text{Fe}_{60}\text{B}_{20}(5)/\text{MgO}(2)/\text{Al}_2\text{O}_3(10)$  were also prepared at the same deposition conditions. Here  $\text{Al}_2\text{O}_3$  acts as capping layer, which stops degradation of  $\text{MgO}$  layer and hence, the CoFeB film with time. The sputter-deposited films were annealed at  $280^\circ\text{C}$  in vacuum under a perpendicular magnetic field of  $600$  mT for  $\approx 1\text{hr}$ . The annealing in vacuum ensured smooth defect-free interfaces with uniform lateral distribution of magnetic properties. In this study  $5$  nm thick CoFeB were intentionally chosen, so that its quality (i.e. roughness) and magnetic properties became independent of underlayer materials. This enabled investigation of the effect of SOC strength of underlayer NM materials on the dynamic parameters of CoFeB, while ensuring other magnetic parameters identical.

# Chapter 6

## Results and discussion

Using the TR-MOKE setup we studied the Kerr rotation signal detected, which is again proportional to the magnetization of the material.

### 6.1 Laser-induced ultrafast magnetization dynamics

As discussed earlier, as the laser pulse interacts with the ferromagnetic thin film, maintained in the saturated state by application of a magnetic field  $H = 1610$  Oe, it demagnetizes the sample which is followed by a fast remagnetization and slow remagnetization and magnetic precession state. After analysing the experimental data, we have found the same. Figure 6.1 shows three different regions in our observed curve.

### 6.2 Fitting of experimental data and analysis of related parameters

#### 6.2.1 Fitting and analysis of demagnetization data

As we have discussed, we can fit the demagnetization data within certain assumptions with the fitting function introduced earlier. Different parameters of the two samples have been analyzed and their dependence on the laser pump fluence of range  $2.8 \text{ mJ/cm}^2$  to  $11.2 \text{ mJ/cm}^2$ .

As we know from previous discussion, the constant,  $A_1$ , indicates the ratio between the amount of magnetization after equilibrium between electrons, spins, and lattice is restored and the initial magnetization.  $A_2$  is proportional to the initial electronic temperature rise. The parameters are

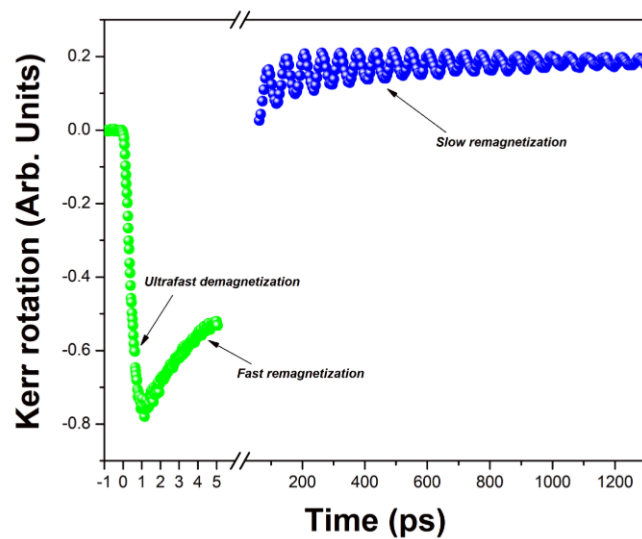


Figure 6.1: LASER induced magnetization dynamics of CoFeB sample

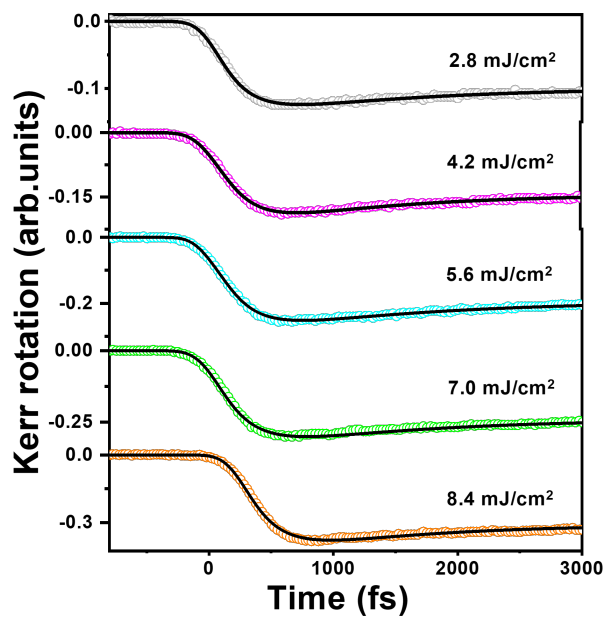


Figure 6.2: Fitting of demagnetization data for various LASER fluences for CoFeB sample

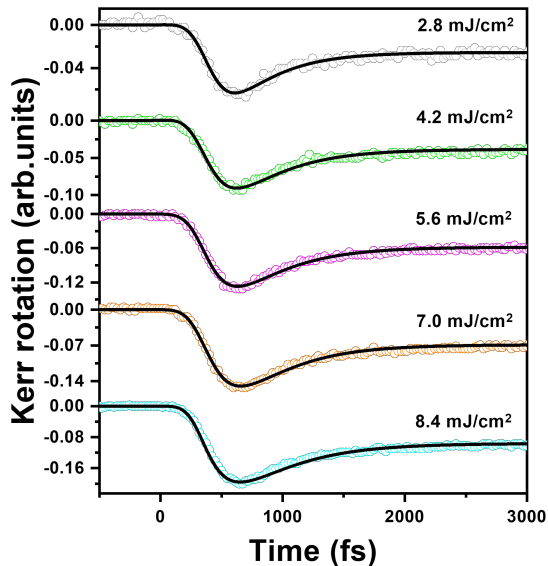


Figure 6.3: Fitting of demagnetization data for various LASER fluences for Pt/CoFeB sample

plotted as a function of laser fluence, values of both of them are found to be decreased with decreased laser fluence for both the samples. With the increase in LASER fluence more energy is deposited to the portion of the sample therefore the intial electron temperature rise should be more with the increasing LASER fluence.

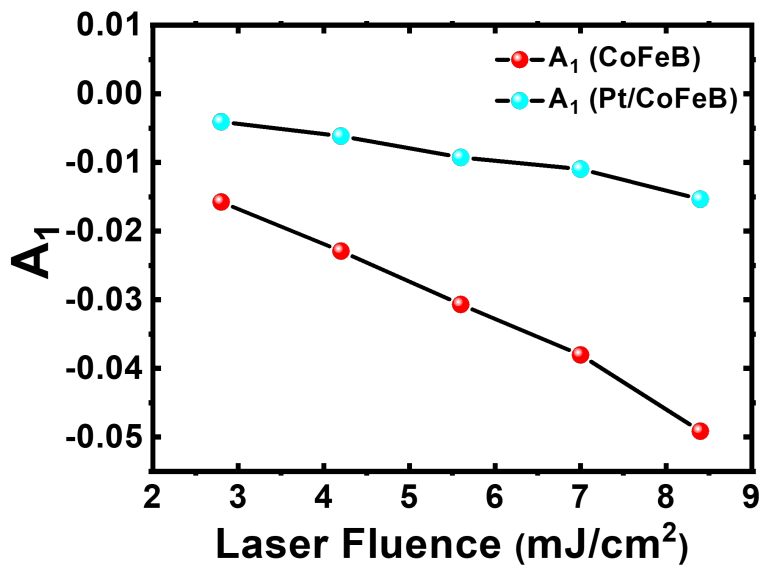


Figure 6.4: Variation of  $A_1$  with laser fluence for CoFeB and Pt/CoFeB sample

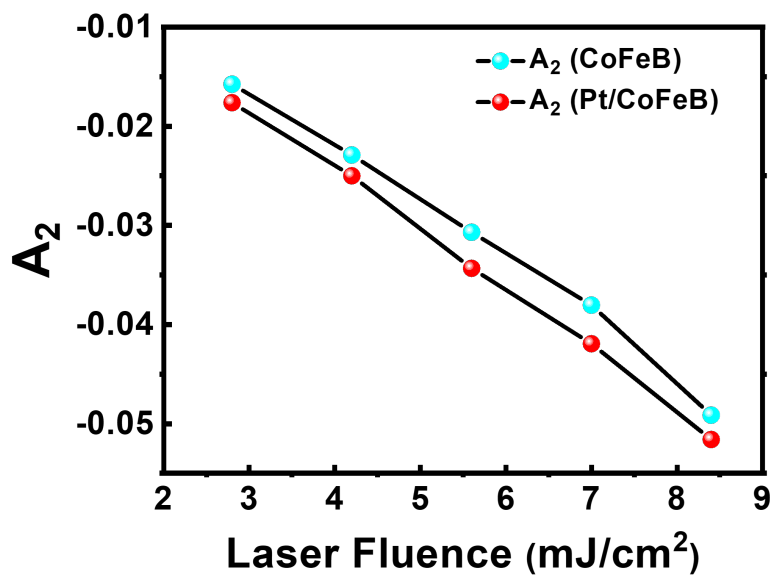


Figure 6.5: Variation of  $A_2$  with laser fluence for CoFeB and Pt/CoFeB sample.

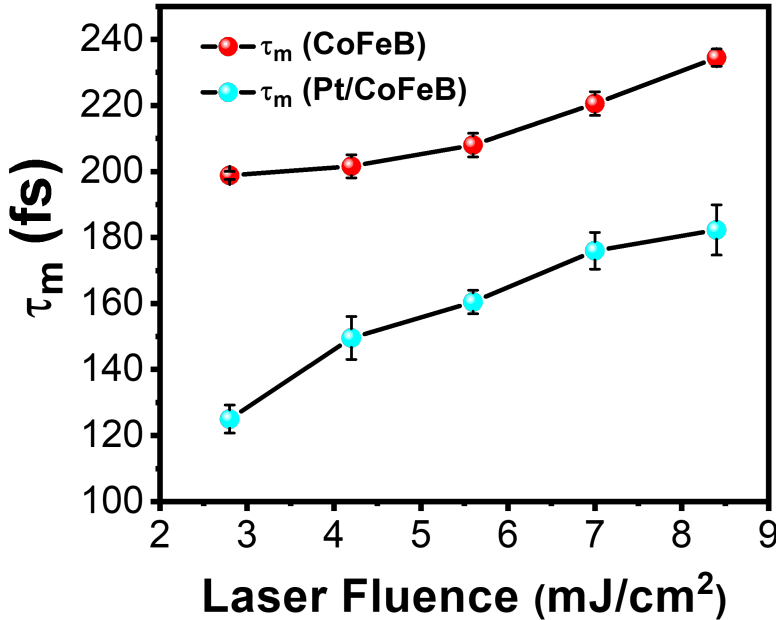


Figure 6.6: Comparison of LASER fluence dependence of the demagnetization time

This trend is observed because with the increase in LASER fluence more energy deposition causes the system to take more time in order to get transferred the energy to the spin system as a result of spin flip scattering therefore the magnetization of the sample decreases which takes more time. For Pt/CoFeB the demagnetization time is less as there is extra channel for the spin transport i.e. the heavy metal layer of Pt, as some experimental study shows that CoFeB has a significant partial density of states (pDOS) below  $E_F$  that can be excited by the laser pump, and even has a larger pDOS than Pt around  $E_F$  because the Pt 5d bands lie at lower energies than the CoFeB 3d bands, which provide the main part of the DOS at  $E_F$ . This implies that spin-majority electrons of Fe 3d states will be excited to Pt states either immediately through optical intersite electron transfer or by initial excitation to unoccupied Fe states followed by hot electron hopping to Pt sites as in superdiffusive transport, and as a result the demagnetization happens in a faster process than the CoFeB sample (Figure 6.6). On the other hand, fast remagnetization time is found to remain almost constant within the experimental fluence range of  $2.8 - 11.2 \text{ mJ}/\text{cm}^2$  as shown in figure 6.7.

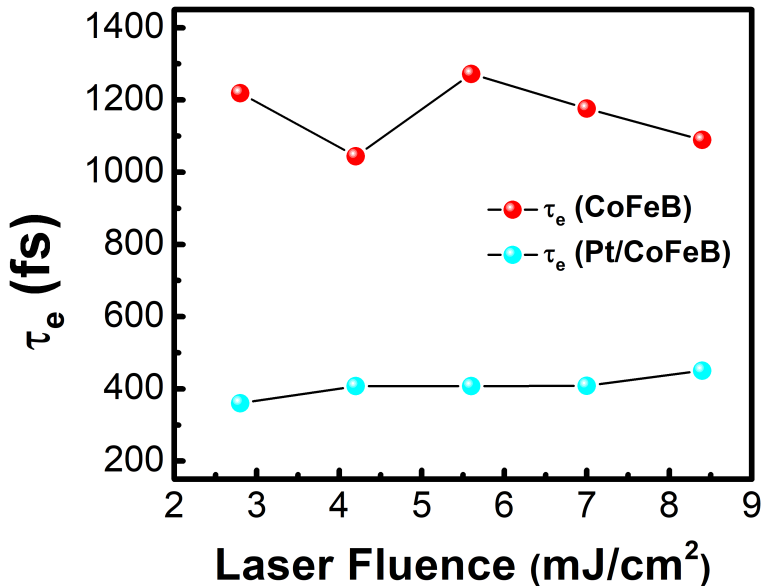


Figure 6.7: Comparison of LASER fluence dependence of the fast remagnetization time

## 6.3 Fitting and analysis of precessional data

### 6.3.1 Field dependent precessional data

Slow remagnetization superposed with damped precession within the time window of 1.6 ns. We process the magnetization precession part after subtracting a bi-exponential background to estimate the damping and its modulation. The slower remagnetization is mainly due to heat diffusion from the lattice to the substrate and the surroundings. Within our experimental fluence range, the slow remagnetization time increases. The precessional dynamics is described by the phenomenological LLG equation, as discussed earlier. Following figure shows the background subtracted time-resolved Kerr rotation data (precessional part) for different pump fluences fitted with a damped sinusoidal function,  $Ae^{-t/\tau} \sin(2\pi ft + \phi)$ . Where A,  $\tau$ , f and  $\phi$  are the amplitude of the magnetization precession, the relaxation time, the initial precessional frequency and the initial phase respectively.

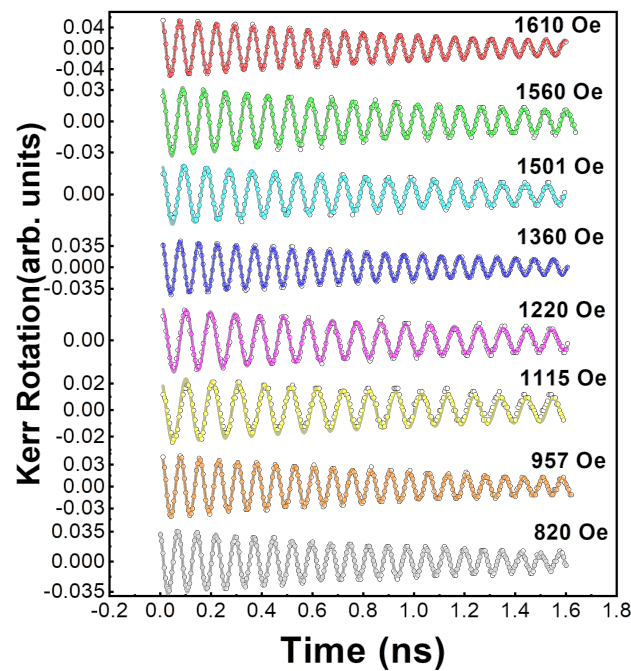


Figure 6.8: Determination of the average precessional frequency from the precessinal datas for various bias field for CoFeB sample.

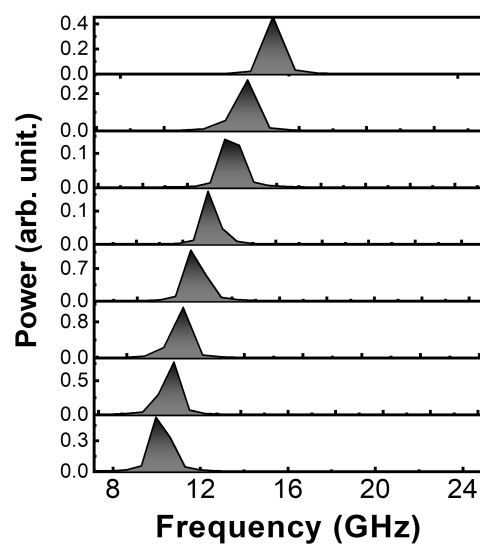


Figure 6.9: The FFT of precessinal datas for various bias field for CoFeB sample

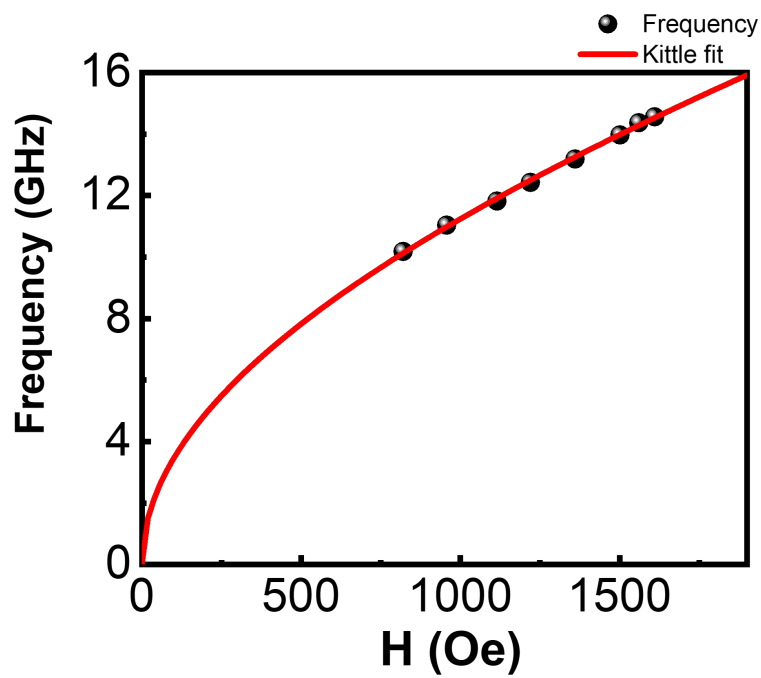


Figure 6.10: Change in average frequency with bias field (Red line shows the kittle fitting)

From the Kittel fit the value of  $M_{\text{eff}} = 1201.67589 \text{ emu/cc}$ .

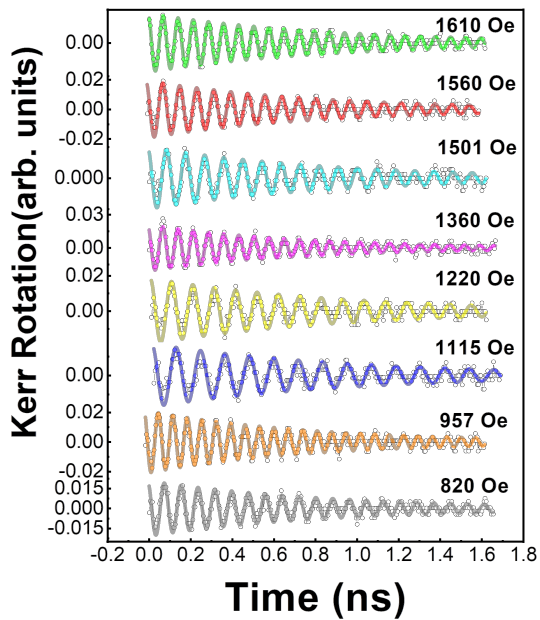


Figure 6.11: Determination of the average precessional frequency from the precessinal datas for various bias field for Pt/CoFeB sample

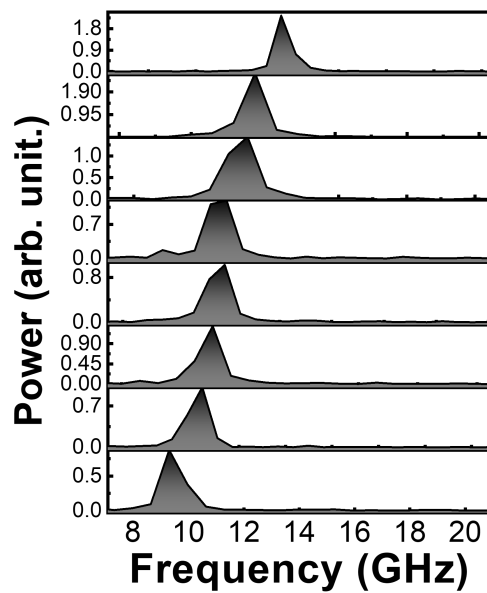


Figure 6.12: The FFT of precessinal datas for various bias field for Pt/CoFeB sample.

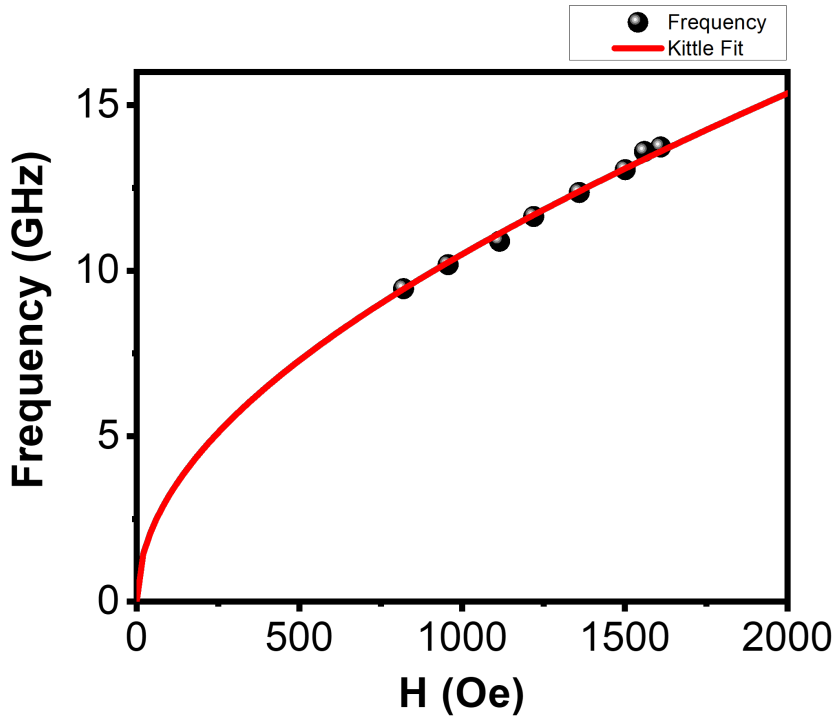


Figure 6.13: Change in average frequency with bias field (Red line shows the Kittel fitting)

From the Kittel fit the value of  $M_{\text{eff}} = 1037.75535 \text{ emu/cc}$ .

As we can see the effective Gilbert damping parameter does not change significantly for both the samples with applied field (Figure 6.14), which implies that the extrinsic effect like two magnon scattering and spin dephasing are not responsible for the damping. Also it is observed that the effective damping of Pt/CoFeB is greater than that of the CoFeB sample (Figure 6.14) this is because of adding the Platinum layer due to spin pumping, interfacial d-d hybridization the spin gets transported to the Platinum layer causing the magnetization precession to relax faster and get aligned to the effective magnetic field direction.

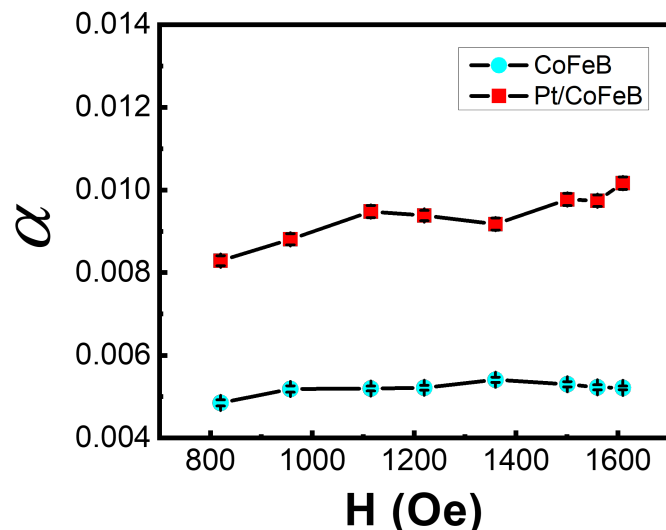


Figure 6.14: Variation of effective damping parameter with applied field for CoFeB and Pt/CoFeB sample

Relaxation time variation has also been plotted (Figure 6.15) as we can see the relaxation time is more for CoFeB than the Pt/CoFeB as we have

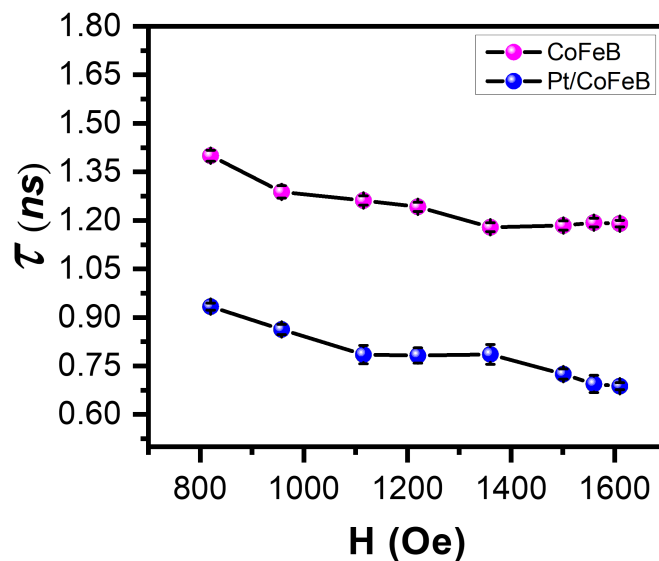


Figure 6.15: Variation of relaxation time with applied field for CoFeB and Pt/CoFeB sample.

discussed. Also it is found that the relaxation time does not show any particular trend with increase in the applied field value. Which implies that the relaxation of the magnetization precession is not dependent on some extrinsic effect.

### 6.3.2 Fluence dependent precessional data

Here the precessional data of both CoFeB and Pt/CoFeB sample and how the different parameters vary with the laser pump fluence of range  $2.8 \text{ mJ/cm}^2$  to  $11.2 \text{ mJ/cm}^2$ .

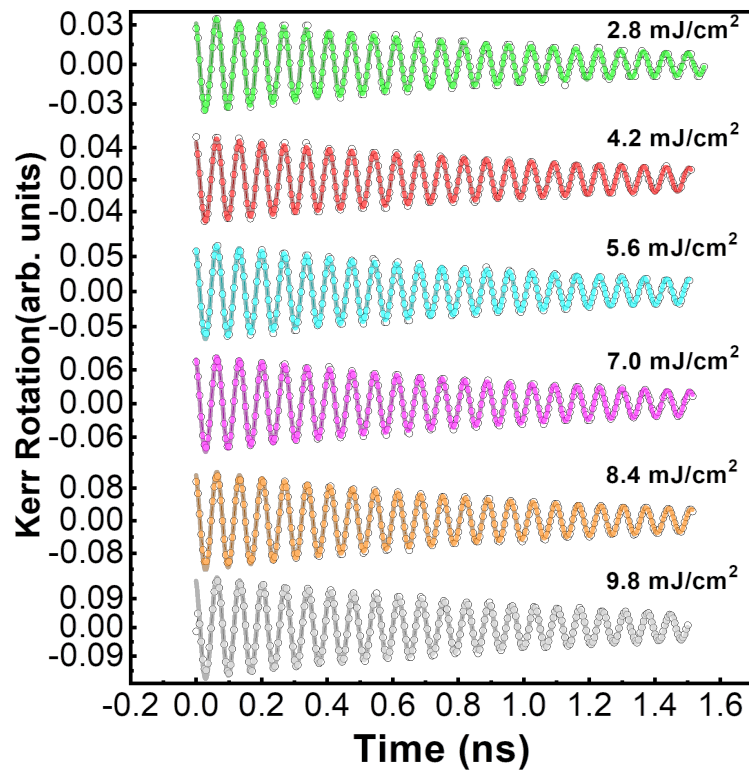


Figure 6.16: Background-subtracted time-resolved Kerr rotation data for different pump fluences at  $H_0 = 1610 \text{ Oe}$ , for the CoFeB sample here solid lines are fitting lines

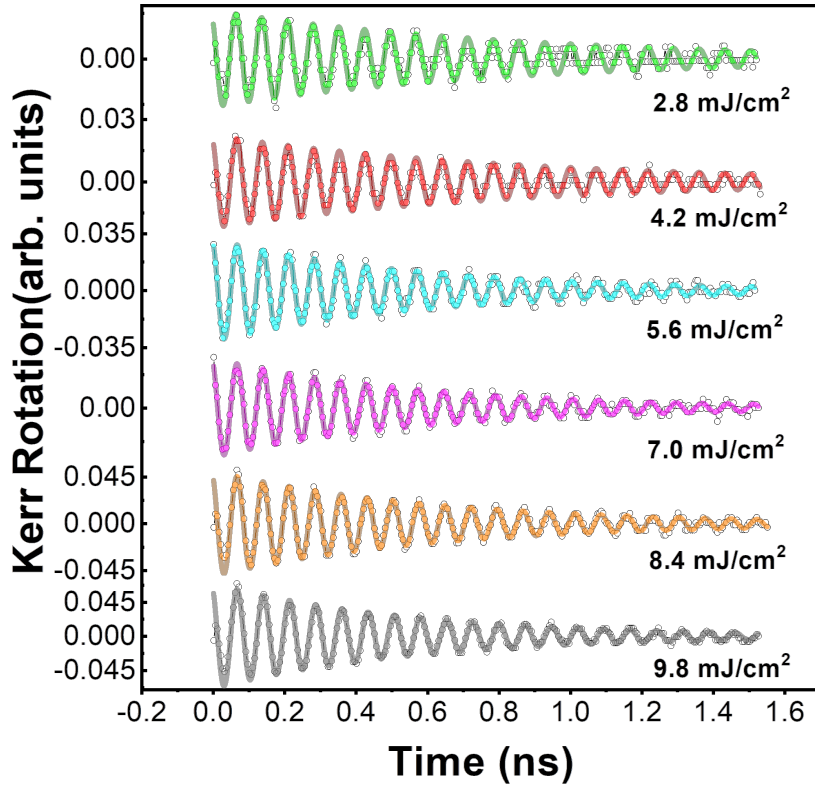


Figure 6.17: Background-subtracted time-resolved Kerr rotation data for different pump fluences at  $H_0 = 1610$  Oe, for the Pt/CoFeB sample here solid lines are fitting lines

From the analysis, it is found that with increasing fluence, the precessional frequency experiences a redshift. We can see that in figure 6.18.

As we can see the precessional frequency changes with the LASER fluence because energy deposited by laser modifies local magnetic properties, i.e. magnetic moment, anisotropy, coercivity, magnetic susceptibility, etc therefore precessional frequency changes as well. Also as time progresses and magnetization of the sample gradually attains its equilibrium value, the precessional frequency continuously changes which is described by a chirping parameter however we have not considered this frequency chirping in our case.

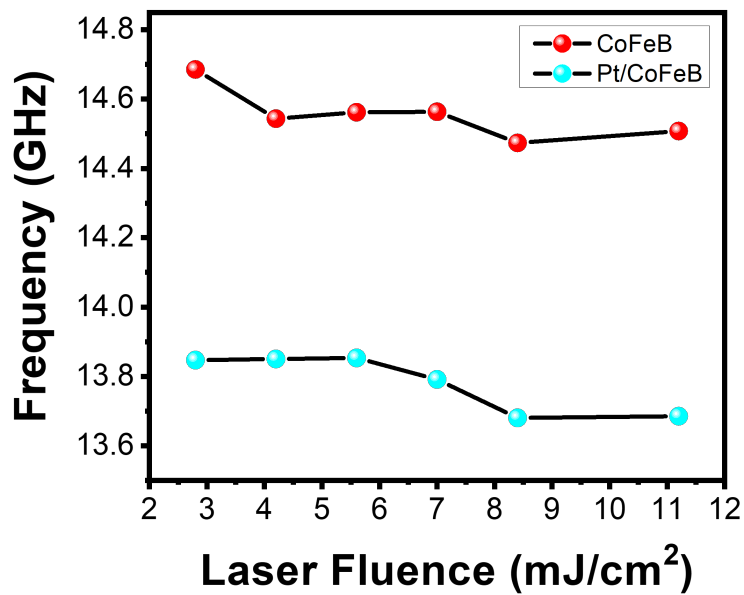


Figure 6.18: Variation of precessional frequency with LASER fluence for both the sample CoFeB and Pt/CoFeB

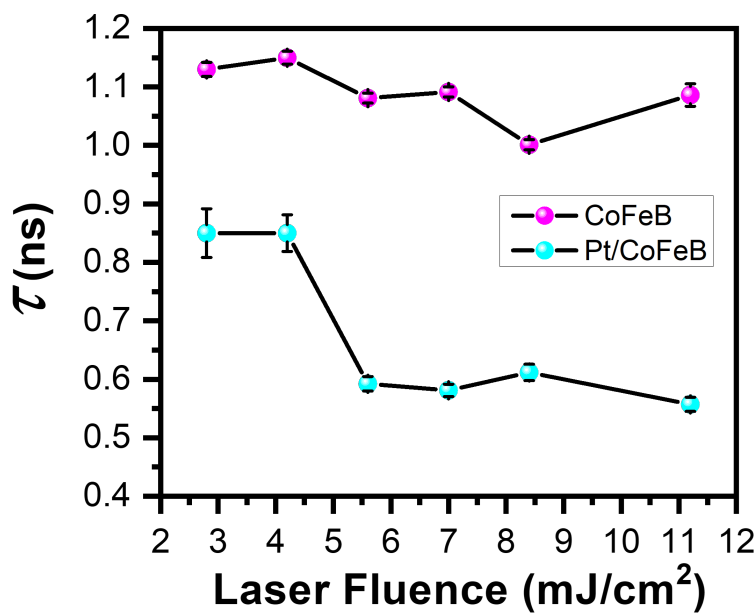


Figure 6.19: Variation of relaxation time with LASER fluence for the CoFeB and Pt/CoFeB sample.

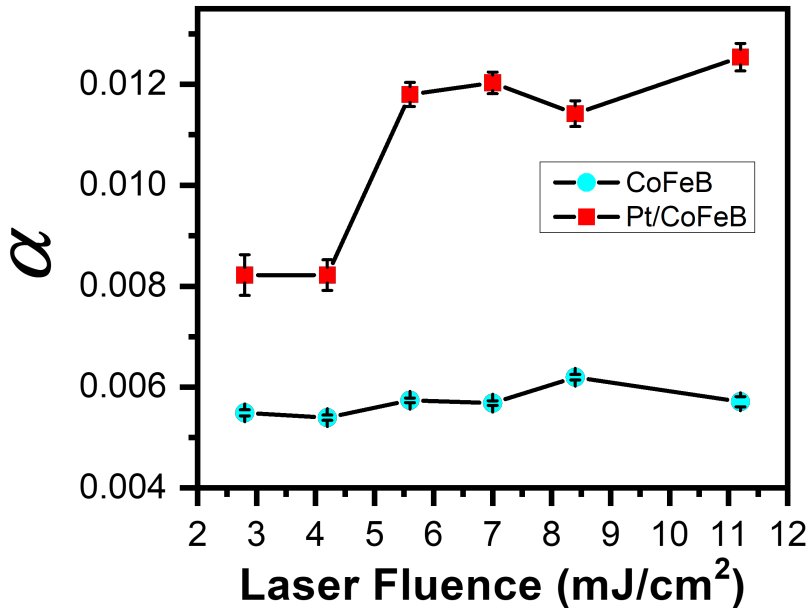


Figure 6.20: Variation of effective damping parameter with LASER fluence for the CoFeB and Pt/CoFeB sample.

With the increase in LASER fluence more energy is being deposited therefore the lattice temperature increases more due to the energy dissipation from the spin to the lattice system. Now further damping is proportional to susceptibility which increases with the lattice temperature. This explains the observed trend in effective damping parameter for both sample CoFeB and Pt/CoFeB with the increase in LASER fluence. We can also see that the effective damping parameter value for the Pt/CoFeB sample is more than the CoFeB sample which is due to the fact that with the inclusion of the Platinum layer to the CoFeB thin film at the interface various phenomena including spin accumulation, spin pumping, spin-orbit coupling, interfacial d-d coupling etc. takes place as a result of the high spin transparency of the Platinum (Pt) the spins accumulated at the interface gets transported to the heavy metal layer this phenomena is known as spin pumping this happens due to the precession of magnetization in the ferromagnetic layer that induces a spin current perpendicular to the interface plane, as a result the precession of the magnetization gets damped out faster, also as we have seen the spin current has the similar form as the LLG equation the gilbert damping parameter gets modified depending on the spin mixing conductance of the material. Also the interfacial d-d coupling enhances the gilbert damp-

ing parameter but here we can not draw a conclusion which effect is more dominating as we have not done that much extensive study.

# Chapter 7

## Conclusion

In this project we see from the analysis of TR-MOKE data for ferromagnetic thin films that with the use of LASER pulse a ultrafast demagnetization and remagnetization along with precession occurs within 2ns time scale. From the fluence dependent study of the CoFeB and Pt/CoFeB thin film we could see the correlation between ultrafast demagnetization time and LASER fluence. Also how Platinum layer affects the demagnetization time. From the field dependence data we could determine the value of effective magnetization, as well as we could find out how relaxation time and effective Gilbert damping parameter does not change much with the field value.

From the fluence dependence data we studied that the precessional frequency gets red shifted and the for both the sample and relaxation time decreases with increase in LASER fluence also we could find that the effective Gilbert damping parameter increases with the increase in LASER fluence. That is, the more spin current transferred from the ferromagnetic layer to normal metal, the faster the ultrafast demagnetization should be. The spin currents at the femtosecond time scale give rise to a lowering of the demagnetization time, while spin-pumping-induced spin current gives rise to the enhancement of Gilbert damping and thus a lowering of the relaxation time [10].

Comparing the fluence dependent data for the CoFeB and Pt/CoFeB sample we could give a possible explanation of the observed trend in the various parameter values. From this comparative study we could analyse the effect of inclusion of a heavy metal layer to the ferromagnetic thin film and we could see the damping can be modified by this. However for the practical situation we often need to control damping as we have discussed earlier that can be done in several ways among which the dynamic control of damping

is most important as in this process by sending electrical current we can regulate the damping for this we can use spin hall effect which arises due to spin orbit coupling. These are the future scope of this particular study of the effect of adding a heavy metal layer to the ferromagnetic thin film.

# References

- [1] N. A. Spaldin, *Magnetic Materials: Fundamentals and Applications*. Cambridge University Press, 2 ed., 2010.
- [2] X. Zhang, “Dynamics of magnetic skyrmions in nanostructures and their applications.” [https://soar-ir.repo.nii.ac.jp/record/20148/files/18TR0001\\_ronbun.pdf](https://soar-ir.repo.nii.ac.jp/record/20148/files/18TR0001_ronbun.pdf), 2018.
- [3] T. Moriya, “Anisotropic superexchange interaction and weak ferromagnetism,” *Physical review*, vol. 120, no. 1, p. 91, 1960.
- [4] A. Fert, N. Reyren, and V. Cros, “Magnetic skyrmions: advances in physics and potential applications,” *Nature Reviews Materials*, vol. 2, no. 7, pp. 1–15, 2017.
- [5] A. Akbari, I. Eremin, and P. Thalmeier, “RKKY interaction in the spin-density-wave phase of iron-based superconductors,” *Physical Review B*, vol. 84, no. 13, p. 134513, 2011.
- [6] A. Barman and J. Sinha, *Spin dynamics and damping in ferromagnetic thin films and nanostructures*, vol. 1. Springer, 2018.
- [7] F. Dalla Longa, J. Kohlhepp, W. De Jonge, and B. Koopmans, “Influence of photon angular momentum on ultrafast demagnetization in nickel,” *Physical Review B*, vol. 75, no. 22, p. 224431, 2007.
- [8] S. Panda, S. Mondal, J. Sinha, S. Choudhury, and A. Barman, “All-optical detection of interfacial spin transparency from spin pumping in  $\beta$ -ta/cofeb thin films,” *Science advances*, vol. 5, no. 4, p. eaav7200, 2019.
- [9] C. Kittel, “On the theory of ferromagnetic resonance absorption,” *Physical review*, vol. 73, no. 2, p. 155, 1948.
- [10] W. Zhang, W. He, X.-Q. Zhang, Z.-H. Cheng, J. Teng, and M. Fähnle, “Unifying ultrafast demagnetization and intrinsic gilbert damping in

co/ni bilayers with electronic relaxation near the fermi surface,” *Physical Review B*, vol. 96, no. 22, p. 220415, 2017.